Mechanical loading reveals an intrinsic cardiomyocyte stiffness contribution to diastolic dysfunction in murine cardiometabolic disease

Johannes V. Janssens[1,6], Antonia J.A. Raaijmakers[1], Parisa Koutsifeli[3], Kate L. Weeks[1,4], James R. Bell[1,5], Jennifer E. Van Eyk[6], Claire L. Curl[1], Kimberley M. Mellor[2,3,1] and Lea M.D. Delbridge[1]

[1]Department of Anatomy & Physiology, University of Melbourne, Australia

[2]Department of Physiology, University of Auckland, New Zealand

[3]Auckland Bioengineering Institute, University of Auckland, New Zealand

[4]Baker Department of Cardiometabolic Health (Baker), University of Melbourne, Australia

[5]Department of Microbiology, Anatomy, Physiology & Pharmacology, La Trobe University, Australia

[6]Smidt Heart Institute, Cedars-Sinai Medical Center, Los Angeles, USA.

Running Title: *Cardiomyocyte stiffness in diastolic dysfunction*

Key words: *cardiomyocyte; diastolic dysfunction; cardiometabolic disease; stiffness; relaxation; Ca^{2+} myofilament interaction*

A draft version of this manuscript was first published as a preprint: Janssens JV et al (2024). [Mechanical loading reveals an intrinsic cardiomyocyte stiffness contribution to diastolic dysfunction in murine cardiometabolic disease] bioRxiv. 2024.02.21.581448; doi: https://doi.org/10.1101/2024.02.21.581448

Corresponding author:

Prof Lea MD Delbridge

Cardiac Phenomics Laboratory

Department of Anatomy and Physiology,

University of Melbourne, Australia.

lmd@unimelb.edu.au

ABSTRACT

Cardiometabolic syndromes including diabetes and obesity are associated with occurrence of heart failure with diastolic dysfunction. There are no specific treatments for diastolic dysfunction, and therapies to manage symptoms have limited efficacy. Understanding of the cardiomyocyte origins of diastolic dysfunction is an important priority to identify new therapeutics. The investigative goal was to experimentally define *in vitro* stiffness properties of isolated cardiomyocytes derived from rodent hearts exhibiting diastolic dysfunction *in vivo* in response to dietary induction of cardiometabolic disease.

Male mice fed a high fat/sugar diet (HFSD vs control) exhibited diastolic dysfunction (echo E/e' doppler ratio). Intact paced cardiomyocytes were functionally investigated in three conditions: non-loaded, loaded and stretched.

Mean stiffness of HFSD cardiomyocytes was 70% higher than control. E/e' for the origin hearts was elevated by 35%. A significant relationship was identified between *in vitro* cardiomyocyte stiffness and *in vivo* dysfunction severity. With conversion from non-loaded to loaded condition, the decrement in maximal sarcomere lengthening rate was more accentuated in HFSD cardiomyocytes (vs control). With stretch, the Ca^{2+} transient decay time course was prolonged. With increased pacing, cardiomyocyte stiffness was elevated, yet diastolic Ca^{2+} elevation was attenuated. Our findings show unequivocally that cardiomyocyte mechanical dysfunction cannot be detected by analysis of non-loaded shortening.

Collectively, these findings demonstrate that a component of cardiac diastolic dysfunction in cardiometabolic disease is derived from cardiomyocyte stiffness. Differential responses to load, stretch and pacing suggest that a previously undescribed alteration in myofilament-Ca^{2+} interaction contributes to intrinsic cardiomyocyte stiffness in cardiometabolic disease.

KEY POINTS

- Understanding cardiomyocyte stiffness components is an important priority for identifying new therapeutics for diastolic dysfunction, a key feature of cardiometabolic disease.

- In this study cardiac function was measured *in vivo* (echocardiography) for mice fed a high-fat/sugar diet (HFSD, ≥25weeks). Performance of intact isolated cardiomyocytes derived from the same hearts was measured during pacing under non-loaded, loaded and stretched conditions *in vitro.*

- Calibrated cardiomyocyte stretches demonstrated that stiffness (stress/strain) was elevated in HFSD cardiomyocytes *in vitro* and correlated with diastolic dysfunction (E/e') *in vivo*. HFSD cardiomyocyte Ca^{2+} transient decay was prolonged in response to stretch. Stiffness was accentuated with pacing increase while the elevation in diastolic Ca^{2+} was attenuated.

- Data show unequivocally that cardiomyocyte mechanical dysfunction cannot be detected by analysis of non-loaded shortening.

- These findings suggest that stretch-dependent augmentation of the myofilament-Ca^{2+} response during diastole partially underlies elevated cardiomyocyte stiffness and diastolic dysfunction of hearts of animals with cardiometabolic disease.

78 **INTRODUCTION**

79

80 Increasingly, cardiometabolic syndromes, including diabetes and obesity, are associated with occurrence of
81 heart failure with a diastolic dysfunction patho-phenotype (Sotomi *et al.*, 2021). Diastolic dysfunction is
82 characteristic of heart failure with preserved ejection fraction (HFpEF) which has now overtaken heart
83 failure with reduced ejection fraction (HFrEF) comprising the majority of new heart failure diagnoses
84 (McHugh *et al.*, 2019; Jackson *et al.*, 2022). Diastolic dysfunction is also linked with progression of diabetic
85 cardiomyopathy (Patil *et al.*, 2011; Redfield, 2016). With both HFpEF and diabetic heart disease, early
86 development of diastolic dysfunction can be detected even when other phenotypic features/comorbidities
87 are heterogeneous (i.e. hypertrophy, dilation, natriuretic factor elevation, hypertension) (Kittleson *et al.*,
88 2023). Common clinical features of cardiometabolic syndromes, including obesity and insulin resistance, are
89 independent risk factors for diastolic dysfunction as a prelude to heart failure (Rozenbaum *et al.*, 2019;
90 Kamon *et al.*, 2020). The experimental induction of these phenotypes using a high/fat sugar diet feeding
91 protocol has been shown by us and others to reliably produce diastolic dysfunction in rodents (Pulinilkunnil
92 *et al.*, 2014; Dia *et al.*, 2020; Sowers *et al.*, 2020; Wingard *et al.*, 2021; Daniels *et al.*, 2022). Cardiometabolic
93 syndromes can involve the 'silent' presence and progression of diastolic dysfunction for an extended
94 period. Symptoms can be subclinical and/or detectable only in challenge conditions (i.e. as reduced
95 diastolic reserve in exercise) or when exacerbated by co-morbidity (Leung *et al.*, 2015; Lam *et al.*, 2019).
96 Diagnosis of heart failure with diastolic dysfunction is independently associated with higher incidence of
97 adverse clinical events (Sotomi *et al.*, 2021). Notably, there is currently no specific treatment for diastolic
98 dysfunction and/or HFpEF, and therapies to manage symptoms have limited efficacy (Delbridge *et al.*,
99 2022).

100

101 In diastolic dysfunction, the relaxation and filling phases of the cardiac cycle are impaired. The condition is
102 generally described qualitatively as an increase in left ventricular wall 'stiffness' (or by a decrease in
103 compliance, the inverse of stiffness) (Daniels *et al.*, 2022; Janssens *et al.*, 2024). Clinically and
104 experimentally, reduced compliance can be measured invasively as an elevation in left ventricular filling
105 pressure or an increase in the gradient of the diastolic pressure-volume relationship. Non-invasively, on
106 doppler echocardiogram, an increase in the E/e' ratio [early (E) mitral valve blood flow rate to early mitral
107 annulus tissue motion (e')] is an index used to identify diastolic abnormality (Lo & Thomas, 2010).

108

109 Myocardial stiffness is commonly considered to reflect myocardial extracellular matrix abnormalities linked
110 with increased tissue fibrosis. While a component of reduced compliance likely reflects fibrotic infiltration,
111 diastolic dysfunction can be identified in settings where there is no evidence of increased interstitial fibrosis
112 burden (Curl *et al.*, 2018). There is growing appreciation that alterations of myocardial compliance in
113 diastolic dysfunction disease states represents underlying intrinsic cardiomyocyte stiffness pathology which

contributes to impaired relaxation and filling (Zhou & Pu, 2016; Villalobos Lizardi *et al.*, 2022). Understanding the cardiomyocyte origin of diastolic dysfunction is an important priority to identify new molecular targets and to support the development of new diagnostics and therapeutics to reduce morbidity and mortality in cardiometabolic disease states.

Cardiomyocyte origins of diastolic dysfunction potentially comprise structural and operational components. Evidence of molecular changes in sarcomeric and cytoskeletal elements is extensive (Villalobos Lizardi *et al.*, 2022; Loescher *et al.*, 2023; Janssens *et al.*, 2024). Operationally, the cardiac cycle of contraction and relaxation is driven by the cyclic flux of cardiomyocyte activator Ca^{2+} to initiate contraction (myocyte sarcomere shortening) and to allow relaxation (myocyte sarcomere lengthening). The relationship between cytosolic Ca^{2+} levels and myofilament activation is dynamic and depends on several external factors some of which include stretch and pacing (Fabiato & Fabiato, 1978; Varian & Janssen, 2007).

Conventionally, the steady-state force-Ca^{2+} analysis (typically performed in permeabilised, quiescent preparations) is used to summarise the myofilament-Ca^{2+} response and is the product of many complex myofilament protein interactions. Less work has been done to investigate the dynamic changes in the myofilament-Ca^{2+} relationship in paced intact cardiomyocytes, especially in disease contexts. In diastolic dysfunction, specifically in HFpEF animal models, evidence is accruing that Ca^{2+} deficit and impaired non-loaded shortening *are not* phenotypic (Kilfoil *et al.*, 2020). Indeed cardiomyocyte myofilament hyper-activation and elevated Ca^{2+} levels have been reported (Curl *et al.*, 2018; Louch, 2020; Saad *et al.*, 2023). As we have recently proposed, the role for elevated diastolic Ca^{2+} levels and augmented myofilament-Ca^{2+} response comprising a cross-bridge derived component of cardiomyocyte diastolic stiffness is increasingly plausible (Janssens *et al.*, 2024). This experimental enquiry focusses on intact cardiomyocyte mechanical and Ca^{2+} performance in response to load, stretch and modulated pacing conditions.

While the term ‘stiffness’ is used as a general descriptor of impaired compliance in a cardiovascular setting, it is more formally specified quantitatively in physical science disciplines (Mirsky, 1976). Stiffness is defined as the extent to which an object resists deformation. Stiffness is influenced by the geometry and the intrinsic material properties of an object. In the cardiac literature and in this study, stress/strain relations are calculated to assess cardiomyocyte resistance to stretch. Stress is defined as force per cross-sectional area, and strain is the application of a normalized stretch or deformation. The ratio of stress/strain defines the cardiomyocyte resistance to stretch independent of geometry and is known as ‘Young’s Modulus’. While stiffness and Young’s Modulus are not equivalent, the term ‘stiffness’ is commonly used (even though Young’s Modulus is the correct formal term). In the cardiac setting, a stretch or deformation state is commonly described as ‘loading’ – for example ‘pre-load’ (diastolic stretch) and ‘after-load’ (resistance to shortening). Depending on the experimental design, stiffness behaviour of myocardial tissues, active

150 cardiomyocytes and/or myocyte sub cellular cytoskeleton and sarcomere structures all potentially
151 contribute to *in vivo* functional stiffness. Little is known about how stiffness measured at different
152 structural levels may determine function *in vivo* and how stiffness elements are quantitatively changed in
153 pathophysiology – in particular in acquired disease conditions. Thus, the goal of this investigation was to
154 experimentally characterize *in vitro* stiffness properties (stress/strain) of cardiomyocytes derived from
155 hearts of animals exhibiting diastolic dysfunction *in vivo* in the setting of dietary induction of
156 cardiometabolic disease.
157

158 **METHODS & MATERIALS**

159

160 **Ethical approval**

161 The authors understand the ethical principles under which *The Journal of Physiology* operates, and the
162 work presented in this study complies with the animal ethics checklist as outlined in Instructions to
163 Authors. All experiments conform to the principles and regulations as described by Grundy (2015). Animals
164 (male C57Bl/6J mice) were purchased from the Animal Resource Centre (Perth, WA Australia). All animal
165 experiments were approved by the University of Melbourne (School of Biomedical Sciences) Animal Ethics
166 Committee (Project Ethics Approval 10366) and complied with the guidelines and regulations of the Code of
167 Practice for the Care and Use of Animals for Scientific Purposes (National Health and Medical Research
168 Council Australia). Animals were provided with free access to food and water, were group housed in a
169 temperature-controlled environment 21-23°C with 12 hour light/dark cycles. Animals were euthanised
170 under anaesthesia (single dose of sodium pentobarbital 70 mg/kg i.p) on cardiac excision.
171

172 **Animal model of cardiometabolic disease**

173 As a pre-clinical cardiometabolic disease model, the high fat/sugar diet (HFSD) fed rodent recapitulates a
174 common and growing human disease phenotype (obesity, insulin resistance, glucose intolerance) and has
175 been established as a diastolic dysfunction model (Heather *et al.*, 2022). Cardiometabolic disease was
176 induced in male C57Bl/6J mice by a high fat/sugar dietary intervention commencing at 8-9 weeks of age.
177 Animals were randomized to experimental treatment groups and were group housed (> 4 animals per cage)
178 in a temperature-controlled environment 21-23°C with 12 hour light/dark cycles. After 1 week transitional
179 feeding period (alternating feed periods), animals were fed a HFSD (43% kcal from fat, 200 g/kg sucrose,
180 SF04-001, Specialty Feeds) or control reference diet (CTRL: 16% kcal from fat, 100 g/kg sucrose, AIN93G,
181 Specialty Feeds) for at least 25 weeks.
182

183 **Glucose tolerance testing**

184 At 23-25 weeks of feeding, glucose tolerance testing was performed in mice following 6 hours fasting as
185 previously described (Chandramouli *et al.*, 2018). Baseline blood glucose levels were measured using an

186 Accu-Chek glucometer with a blood sample obtained from a needle prick to the tail vein. Glucose (1.5 g/kg
187 body weight) was injected i.p. and blood glucose was measured at 5, 15, 30, 60, 90 and 120 minutes after
188 the glucose injection.
189
190 **Transthoracic echocardiography**
191 At 25-26 weeks of feeding, cardiac structure, systolic and diastolic function were evaluated by transthoracic
192 2-dimensional B- and M-mode and blood flow and tissue doppler echocardiography (GE Vivid 9; 15mHz i13L
193 linear array transducer) as described previously (Chandramouli *et al.*, 2018; Curl *et al.*, 2018). Briefly, mice
194 were lightly anesthetised with Isoflurane (1.5%; Baxter healthcare, Australia). Parasternal short axis view
195 was used to measure morphological and systolic parameters (interventricular septum IVS, left ventricular
196 posterior wall LVPW, left ventricular internal dimension LVID, fractional shortening FS, ejection fraction EF,
197 heart rate HR). Pulse wave Doppler and tissue Doppler scans were acquired from the apical 4 chamber view
198 to assess LV diastolic function parameters: velocity of early (E) and late (A) mitral inflow and early (e') and
199 late (a') diastolic velocity of mitral annulus. From these compound indices of diastolic function E/e', E/A and
200 e'/a' were calculated. In addition, the slope of the E wave was used to calculate mitral valve deceleration
201 time. Three consecutive cardiac cycles were sampled for each measurement.
202
203 **Cardiomyocyte preparation, structural and functional assessment**
204 A series of protocols were implemented to phenotype cardiomyocyte and sarcomere morphology, and
205 assess functional status in different contraction configurations and challenge settings.
206
207 ***Cardiomyocyte isolation, morphology & microfluorimetry.*** Prior to cardiomyocyte isolation animals were
208 aneasthetised (sodium pentobarbital 70 mg/kg i.p) and hearts excised. HFSD and CTRL left ventricular
209 cardiomyocytes were enzymatically isolated using methods previously described (Howlett *et al.*, 2006;
210 Mellor *et al.*, 2011) at 30-32 weeks feeding. Briefly, the heart was excised, cannulated via the aorta, and
211 perfused on a Langendorff apparatus with an oxygenated Ca^{2+} free buffer at 37°C for 10 minutes. The
212 buffer was composed of (in mM): 130 NaCl, 5 KCl, 0.33 NaH_2PO_4; 1 $MgCl_2$, 25 HEPES; 20 Glucose; 3 Na
213 Pyruvate; 1 Na Lactate. The Ca^{2+} free buffer was then supplemented with 0.66mg/mL collagenase
214 (Worthington; Type II), 0.033 mg/mL trypsin and 0.05 mM $CaCl_2$ and perfusion continued for a further 10
215 minutes. The heart was removed from the Langendorff apparatus, and the left ventricle was segmented
216 into small pieces in a high potassium solution composed of (in mM): 30 KCl, 90 KOH, 30 KH_2PO_4, 3 $MgSO_4$,
217 50 glutamic acid, 20 taurine, 0.5 EGTA, 10 glucose, and 10 HEPES. Single left ventricular cardiomyocytes
218 were isolated via gentle trituration. Viable cardiomyocytes were resuspended in HEPES-Krebs buffer (in
219 mM); 146.2 NaCl, 4.69 KCl, 0.35 $NaH_2PO_4H_2O$, 1.05 $MgSO_47H_2O$, 10 HEPES, 11 glucose containing 1.8 mM
220 Ca^{2+} and were stored on a rocking platform at room temperature. From each heart cell dimensions were
221 collected from at least 50 rod shaped cardiomyocytes using an inverted light microscope (Nikon) and

222 calibrated eye piece as previously described (Curl *et al.*, 2018). Cardiomyocyte volume was calculated by
223 inserting experimentally determined myocyte length and width values into the formula: volume = length x
224 width x depth x multiplier 0.54 (elliptical area of the rectangle defined by width & length, (Satoh *et al.*,
225 1996)). Cardiomyocyte width: depth ratio was assumed to be 1.44 (Natali *et al.*, 2001). Cardiomyocyte
226 cross-sectional area (CSA) could be calculated from measured width scaled for 2-dimensional geometry
227 (CSA = W [W/1.44] x 0.54 μm^2). An aliquot of isolated cardiomyocyte suspension was pipetted into a cell
228 chamber mounted on the stage of an inverted fluorescence microscope (Motic AE31) and superfused with
229 HEPES-Krebs solution with 2 mM Ca^{2+}, 37°C at a flow rate of 2 mL/min. Cardiomyocyte sarcomere length
230 and Ca^{2+} transients were simultaneously recorded during isotonic contractions. Myocyte force development
231 was evaluated in the same cells with transducer attachment, using four protocols described below.
232
233 ***Characterizing cardiomyocyte diastolic function: non-loaded shortening measurements (isotonic), loaded***
234 ***force measurements (auxotonic), stretch responses and pacing challenge.*** Cardiomyocyte performance
235 was evaluated in several paced conditions: designated 'non-loaded' (isotonic), 'loaded' (auxotonic after-
236 loaded), and 'stretched'(auxotonic pre-loaded). The non-loaded state refers to the absence of externally
237 applied load (noting that sarcomeric and cytoskeletal structures do constitute an underlying internal load).
238
239 Firstly, cardiomyocyte non-loaded (isotonic) sarcomere contractions (IonOptix SarcLen, Fast Fourier
240 Transform, FFT) and Ca^{2+} transients (Fura2-AM, 5 µM microfluorimetry F340:380 nm ratio) were
241 simultaneously measured at 2 Hz, using a microscope diaphragm to define a rectangular intra-myocyte
242 region of interest as depicted. During contraction cycles, cardiomyocyte sarcomere length was monitored
243 within an intracellular region of interest defined by an adjustable diaphragm mounted in the microscope
244 optical tube (**Fig 4A**).
245
246 Secondly, to obtain loaded (auxotonic) contraction data, each cardiomyocyte was attached to a pair of glass
247 fibres coated with a bio-adhesive (MyoTak, IonOptix, USA). Attachment sites were positioned to be outside
248 the sarcomere tracking region, closer to myocyte longitudinal ends. One glass fibre was connected to a
249 force transducer (fibre stiffness 20 N/m, IonOptix, USA), and the other to a piezo-motor (Nano-drive, Mad
250 City Labs Inc. WI, USA) to adjust cardiomyocyte length (**Fig. 4A**). With successful attachments,
251 cardiomyocytes were lifted from the coverslip using motorised micromanipulators (MC1000E, Siskiyou
252 Corporation, USA) attached to both the force transducer and the piezo-motor. Baseline loaded contractions
253 at 2 Hz were recorded. Sarcomere length changes were measured using FFT as described above. In
254 addition, with glass fibre attachment, tracking of mean sarcomere shortening within a myocyte segment
255 delineated by the glass fibre edge positions could be performed in parallel (**Fig4B-C**).
256

Thirdly, force was recorded during a standardized stretch protocol of loaded cardiomyocytes to measure the effect of increasing diastolic cardiomyocyte/sarcomere basal length during pacing. A stress-length relation was constructed for each myocyte (where stress = force/cross-sectional area). Prior to the commencement of the myocyte stretch measurements a protocol to calibrate the stretch step was implemented. Four consecutive 0.5 V input signals were delivered to the piezo-motor to determine a calibration constant to define the percentage cell stretch for a given voltage (**Fig. 4B**). For each myocyte a *Calibration Constant* was calculated as: *myocyte segment length change per piezo-motor mV / sarcomere count in segment* [where *myocyte sarcomere count = myocyte segment length (µm) / average diastolic sarcomere length (µm)*]. To track the glass fibre position a real-time contrast detection algorithm (IonOptix - EdgeLength) was focused on the internal edge of each of the glass fibres (**Fig. 4**) (Peyronnet *et al.*, 2017). This enabled reproducible and comparable stretch steps to be applied to different cardiomyocyte preparations (**Fig. 4B-C**). Prior to the 'stress-length' protocol, a cell-specific calibration constant was applied to yield a standardised stretch for each cardiomyocyte evaluated. The stress-length protocol involved progressive stretch steps totaling an approximate 30% cell stretch (**Fig. 4B-C**).

Lastly, the pacing was increased to 4 Hz, a rate adaptation period allowed (2 min) and the stress-length protocol was repeated. Sarcomere length, force development and intracellular Ca^{2+} transients were simultaneously measured. An average of at least 10 twitches or transients were used to calculate sarcomere, Ca^{2+} and force parameters at a given stretch length. In summary, the following parameters were measured: diastolic stress (mN/mm^2), diastolic stress-length relation [(mN/mm^2) / (%$^-$ length change)], diastolic stress-sarcomere length relations ((mN/mm^2) / µm), systolic : diastolic stress-sarcomere relation (Frank Starling Gain Index (Bollensdorff *et al.*, 2011)), systolic : diastolic stress-length relation, systolic stress amplitude (mN/mm^2), sarcomere shortening (% diastolic SL), maximum sarcomere shortening and lengthening velocity (µm/s). In addition, Ca^{2+} parameters were measured: diastolic Ca^{2+}, systolic Ca^{2+} and time constant of decay of the Ca^{2+} transient (tau).

Statistical analyses

Data are presented as mean ± standard deviation and statistical analysis was performed using GraphPad Prism V9.5.1. Cardiomyocyte stress-length and stress-SL relations were modelled with simple linear regression. For comparison between two groups an unpaired student t-test was used. For assessment between two groups at multiple points a one-way ANOVA with Bonferroni multiple comparisons post-hoc test was used. Two-way ANOVA with Šídák's multiple comparisons post-hoc test was used for the evaluation of data groups with two independent variables. Pearson Correlation analyses were used to assess statistical significance of fitted linear regression lines. A p-value of <0.05 was considered statistically significant. Analyses were performed using a blinded protocol.

293 **RESULTS**

294

295 **Systemic indicators of cardiometabolic disease and *in vivo* diastolic function in HFSD mice**

296 High fat/sugar diet-fed mice exhibited obesity and glucose intolerance. Relative to CTRL, the body weight of
297 HFSD mice was significantly elevated within 5 weeks of dietary intervention increasing over the study
298 duration by 50% relative to CTRL (**Fig. 1A**, CTRL: 28.1±2.0 vs. HFSD: 44.3±1.9 g). After 23-24 weeks diet
299 treatment, glucose tolerance testing of a subset of the HFSD cohort was performed. Glucose intolerance in
300 response to intraperitoneal glucose administration was evidenced by increased area under the curve,
301 consistent with literature reporting insulin resistance in mice fed a similar diet (**Fig. 1B**).

302

303 After confirming these key cardiometabolic disease characteristics in the HFSD mice, echocardiographic
304 functional evaluation was undertaken. Focusing on diastolic function evaluation (**Fig. 1C-G**), there was
305 higher early mitral inflow (**Fig. 1D,** E wave, CTRL: 472±74, HFSD: 569±65 mm/s) and reduced velocity of wall
306 motion (**Fig. 1E,** e' wave, CTRL: 28.5±5.1, HFSD: 25.2±3.5 mm/s) in HFSD myocardium. Deceleration time of
307 mitral inflow was shortened (**Fig. 1F,** CTRL: 30.8±8.7, HFSD: 19.7±5.9 ms) and E/e' ratio increased (**Fig. 1G,**
308 CTRL: 16.7±3.9, HFSD: 22.3±6.0), all observations consistent with reduced tissue compliance and diastolic
309 dysfunction. No significant differences in systolic performance parameters were observed (**Table. 1**),
310 confirming the primary *in vivo* phenotype of diastolic dysfunction. The next step was to evaluate the
311 cardiomyocyte involvement in dysfunction.

312

313 **Non-loaded sarcomere and Ca^{2+} dynamics in CTRL and HFSD cardiomyocytes**

314 Single isolated cardiomyocytes were prepared from hearts of a subset of mice which underwent
315 echocardiographic analyses. For intact, non-loaded cardiomyocytes sarcomere shortening and lengthening
316 cycles were similar for CTRL and HFSD groups (**Fig. 2A**). Diastolic sarcomere length (SL) (**Fig. 2B**, CTRL:
317 1.71±0.04, HFSD: 1.72±0.04 µm) and extent of sarcomere shortening (**Fig. 2C**, CTRL: 3.79±2.24, HFSD:
318 3.94±3.15 % diastolic SL) were not significantly different between groups. Examination of sarcomere
319 contraction kinetics (**Fig. 2D** exemplar trace) showed that the maximum rate of lengthening (**Fig. 2E**, CTRL:
320 1.08±0.85, HFSD: 1.29±1.07 µm/s) and shortening (**Fig. 2F**, CTRL: -2.32±1.44, HFSD: -2.57±2.01 µm/s) did
321 not significantly differ between CTRL and HFSD groups. Collectively these findings indicate that in the non-
322 loaded setting no differences in CTRL and HFSD cardiomyocyte systolic and diastolic non-loaded
323 performance were detected, a finding consistent with other studies investigating non-loaded
324 cardiomyocyte performance in diet-induced cardiometabolic disease including our previous studies in
325 fructose-fed mice (Mellor *et al.*, 2012; Llano-Diez *et al.*, 2016; West *et al.*, 2019; Wang *et al.*, 2020).

326

327 Next, Ca^{2+} parameters were compared with cardiomyocyte sarcomere lengthening performance during
328 relaxation and diastole (**Fig. 2G**, exemplar traces). No significant difference was evident between dietary

329 treatment groups in the systolic Ca^{2+} (**Fig. 2H**, CTRL: 1.098±0.169, HFSD: 1.171±0.182 $F_{340:380}$), diastolic Ca^{2+}
330 (**Fig. 2I**, CTRL: 0.749±0.097, HFSD: 0.761±0.094 $F_{340:380}$) or time constant (tau) of Ca^{2+} transient decay (**Fig.2J**,
331 CTRL: 0.160±0.067, HFSD: 0.137±0.054 sec). Thus, the significant diastolic dysfunction measured *in vivo* for
332 the HFSD group was not observed in a non-loaded *in vitro* setting. To reconcile the impaired
333 echocardiographic heart performance with absence of dysfunction in non-loaded contracting single
334 cardiomyocytes, the next strategy was to assess single cardiomyocyte response to loading. A common
335 feature of cardiometabolic disease is elevation in after-load – i.e. elevated systemic resistance potentially
336 impeding myocardial pump function. To simulate this *in vitro*, mechanically loaded cardiomyocyte
337 performance was examined.
338
339 **Loaded cardiomyocyte sarcomere shortening and lengthening**
340 Immediately after non-loaded cardiomyocyte recordings, glass fibres were attached to cardiomyocyte
341 longitudinally separated positions to permit auxotonic, loaded contraction measurements. For cells
342 successfully attached, the mean difference in sarcomere length measured pre- and post-conversion to
343 loaded mode was <0.02% diastolic length, indicating non-loaded and loaded sarcomere initial lengths were
344 well matched. For attached cardiomyocytes, a comparison of sarcomere shortening behavior in the loaded
345 state could be made (using FFT) to directly match with data obtained non-loaded state.
346
347 In the first instance, data from all myocytes were pooled to investigate the general effects of load
348 regardless of treatment group. With loading, for all myocytes (both treatment groups), extent of sarcomere
349 shortening was reduced and shortening and lengthening kinetics slowed when compared with non-loaded
350 performance (**Fig. 3A**). Mean data showed that in response to loading, sarcomere shortening was reduced
351 by ~34% (**Fig. 3B**, non-loaded: 0.075±0.042, loaded: 0.050±0.031 µm). Maximum rate of shortening was
352 decreased by 58% (non-loaded: -2.85±1.40, loaded: -1.20±0.89 µm/s; not shown), and maximum rate of
353 lengthening by 66% (**Fig. 3C**, non-loaded: 1.46±1.03, loaded: 0.52±0.50 µm/s). The magnitude of the change
354 in extent of shortening and maximum rate of lengthening with loading were positively correlated (**Fig. 3D**)
355 suggesting the possibility of common underlying mechanisms.
356
357 To assess cardiomyocyte rate kinetics in non-loaded and loaded cardiomyocytes independent of shortening
358 extent, the maximum rates of lengthening and shortening were normalised by shortening amplitude to
359 derive 'deformation rate' - i.e. rate of length change, relative to extent of shortening ((µm x sec^{-1})/µm =
360 1/sec). The effect of loading on deformation rate was accentuated in HFSD group (significant ANOVA diet x
361 load interaction effect, **Fig. 3E**). A selective HFSD effect was revealed in the differential between matched
362 'loaded' and 'non-loaded' lengthening cardiomyocytes. The decrement in deformation rate (lengthening)
363 for CTRL and HFSD is shown in **Fig. 3F**, and is accentuated in HFSD in response to loading (CTRL: 6.84±4.08,
364 HFSD: 12.35±7.15 1/s). Treatment differences in deformation rate were not evident during the shortening

365 phase (data not shown)**.** These findings indicated an accentuated influence of load, specific to the
366 lengthening (i.e. diastolic) phase in HFSD cardiomyocytes and could reflect impaired subcellular relaxation
367 processes specific to the HFSD myocardium. Based on these data identifying different CTRL and HFSD origin
368 cardiomyocyte responses in loaded state, we next investigated the effect of stretch applied to
369 cardiomyocytes to simulate *in vivo* 'pre-load' conditions.
370
371 **Cardiomyocyte force development: measuring strain & stress during progressive cardiomyocyte stretch**
372 A hallmark of diastolic dysfunction is an elevated diastolic pressure-volume relationship which describes
373 the increased resistance of the myocardial wall to chamber filling (Aurigemma *et al.*, 2006). We sought to
374 design a single cardiomyocyte version of this relationship (Fowler *et al.*, 2015), by applying standardized
375 stretch steps to cardiomyocytes, defining the steps as a % of non-stretched state (i.e. 'strain'). Diastolic
376 force was measured simultaneously during length stretch steps. The force measured at every strain
377 increment was normalized by cross sectional area (CSA) to produce a measure of 'stress' (i.e. force/CSA,
378 mN/mm^2). Thus a sarcomere 'stress/strain' relation (i.e. force-length) was constructed for each myocyte.
379 The protocols employed to generate stress-strain are depicted in **Fig. 4** and described in detail in the
380 Methods. **Fig. 4** shows the stretch standardization approach used to enable reproducible application of
381 strain (converting voltage signals to linear displacement) as a % length change (via individual myocyte
382 calibration constant calculation) to allow comparisons between different cardiomyocytes. The size of each
383 step change in length on sarcomere length was measured (FFT) and confirmed by tracking the intra-
384 cardiomyocyte segment between the glass fibres (**Fig. 4**). In some cases a direct sarcomere FFT measure
385 was not microscopically resolvable due to myocyte contraction responses which partially positioned some
386 area of the myocyte outside the optimal focal plane. In these situations it was always possible to calculate
387 segment length change. For the example shown, stretch steps were determined to be 2.75µm, and
388 converted to % sarcomere length (i.e. strain) using sarcomere count within intracellular region of interest
389 area (**Fig. 4C**). A comparison of the variability of cell stretches performed using a uniform (pre-set) stretch
390 constant and the individually derived stretch calibration constant demonstrates that reproducibility is
391 optimized with usage of the individual stretch calibration constant data (**Fig. 4D**). Force, sarcomere length
392 and % stretch were measured simultaneously (**Fig. 4**).
393
394 **Quantifying diastolic stiffness in CTRL vs HFSD cardiomyocytes using strain normalization methods**
395 Superimposed exemplar stress recordings are shown in **Fig. 5A** for CTRL and HFSD cardiomyocytes,
396 captured during a series of progressive stretches during a 100 sec period. The dashed (broken) lines are
397 aligned with the diastolic stress step increments for each of the 2 myocytes (using the data points collected
398 prior to the transition to a new step) throughout the series of progressive stretches. A robust increase in
399 systolic force with stretch is also evident, indicative of length-dependent activation, the cardiomyocyte
400 basis for the Frank-Starling mechanism.

401

402 In this experimental setting, stiffness could be visualized as the gradient of the linear plot derived from the
403 cardiomyocyte diastolic stress-length relation. Our stretch protocol methodology provided two approaches
404 for stiffness calculation (as per Methods). A first approach used FFT measurement of sarcomere length to
405 track cardiomyocyte stretch and was plotted according to the standardized stretch steps (in µm). An
406 alternative approach used percent length change calculated as the length of the cardiomyocyte segment
407 between the glass attachment fibres divided by the initial distance between the fibres prior to stretch (in %
408 initial length).

409

410 Applying the first approach, a linear regression was performed to fit the data from which a slope value
411 could be derived. **Fig. 5B** depicts the average diastolic and systolic stress-sarcomere length relations for
412 CTRL cardiomyocytes only. To determine cardiomyocyte diastolic stiffness using FFT-computed sarcomere
413 length values, the gradient of the mean slope of the diastolic stress sarcomere-length relation for each
414 treatment group was calculated, using mean sarcomere length change (µm) as the denominator. This
415 gradient was significantly higher in HFSD myocytes compared to CTRL (**Fig. 5C**). The individual slope
416 gradients were used to calculate the mean diastolic stress / strain gradient (**Fig. 5D,** CTRL: 2.58±2.25, HFSD:
417 5.50±4.01 (mN/mm^2) / µm, p = 0.0996) where there was a trend for a 2.3 fold increase in stiffness of HFSD
418 cardiomyocytes. The statistical power of this analysis was limited due to the difficulty in achieving
419 resolvable diastolic sarcomere lengths by FFT for all myocytes.

420

421 Applying the second approach, it was possible to construct stress-segment length (%) relations for all
422 myocytes from which stress data could be obtained. In **Fig. 5E**, the stress-segment length data for HFSD and
423 CTRL are shown, with a robustly significant difference detected in mean gradient values. In **Fig. 5F** the
424 diastolic stress/strain values calculated for the myocytes from the two treatment groups using this segment
425 approach are directly compared. The HFSD cardiomyocyte stiffness index derived using this approach was
426 increased by 70% compared with CTRL (**Fig. 5F**, CTRL: 0.0075±0.0064, HFSD: 0.0128±0.0068 (mN/mm^2) / %
427 length). There was no significant difference in 'Frank Starling Gain index' (**Table. 2,** CTRL: 2.40±1.06, HFSD:
428 2.77±1.45, (mN/mm^2) / µm) or the ratio of systolic to diastolic stress segment length relations (**Table. 2,**
429 CTRL: 1.62±0.25, HFSD: 1.73±0.50, (mN/mm^2) / % length) indicating that cardiomyocyte length-dependent
430 activation is preserved (Bollensdorff *et al.*, 2011; Najafi *et al.*, 2016)**.**

431

432 To examine the relationship between intrinsic *in vitro* cardiomyocyte stiffness and *in vivo* diastolic
433 dysfunction, diastolic stiffness (slope of the diastolic stress segment-length relation) averaged per animal
434 was plotted against the E/e' index of diastolic dysfunction. There was a significant correlation between
435 cardiomyocyte stiffness and E/e' in HFSD and no evidence of a relationship for the CTRL group (**Fig. 5G**
436 CTRL: p = ns, HFSD: p = 0.0096, r^2 = 0.9213). These data support the interpretation that intrinsic

437 cardiomyocyte stiffness represents a definable and inherent component of diastolic dysfunction occurring
438 *in vivo* in cardiometabolic disease.
439
440
441 **Load dependence of Ca^{2+} transient decay in CTRL and HFSD cardiomyocytes**
442 To further understand the cardiomyocyte functional elements comprising increased intrinsic stiffness in
443 cardiopathology, the relationship between Ca^{2+} transient features and myofilament deactivation in
444 response to progressive stretch was evaluated. In the intact cardiomyocyte model these electro-mechanical
445 coupling processes are functional for interrogation (in contrast to the disrupted cytosolic environment
446 which characterizes permeabilized myocyte preparations). The Ca^{2+} transient decay features were
447 compared for non-loaded and loaded basal states and also in response to progressive stretch.
448
449 In CTRL cardiomyocytes there was no difference in the time constant of Ca^{2+} transient decay (tau, 1/e)
450 between loaded and stretched state (20% increase in length, **Fig. 6A.** loaded 1.18±0.48; stretched
451 1.12±0.35 fold change vs non-loaded reference 1.00±0.46). In HFSD cardiomyocytes the time constant of
452 Ca^{2+} transient decay was increased in stretched cardiomyocytes relative to non-loaded (**Fig. 6A**. non-
453 loaded, 1.00±0.42; loaded 1.22±0.50; stretched 1.42±0.65 fold change). Loading prolonged time to peak
454 Ca^{2+} transient in both CTRL and HFSD cardiomyocytes (**Fig. 6B.** CTRL: non-loaded 1.00±0.25; loaded
455 1.49±0.38; stretched 1.46±0.44, HFSD: non-loaded 1.00±0.41; loaded 1.36±0.41; stretched 1.21±0.34
456 foldchange). The effects can be visualized in **Fig. 6C-D** where the mono-exponential decay of exemplar Ca^{2+}
457 transients is depicted. The shallower decay of the Ca^{2+} transient in the stretched state (**Fig 6D**, HFSD) was
458 apparent whereas the loaded and non-loaded decay traces were virtually overlayed for CTRL
459 cardiomyocytes (**Fig. 6C**). These data suggest that stretch may enhance a mechanism by which the
460 myofilaments bind Ca^{2+} for a prolonged duration during relaxation thus reducing Ca^{2+} availability for
461 extrusion from the cytosol.
462
463 **Pacing-induced $[Ca^{2+}]_i$ increase to examine potential for a cross-bridge derived stiffness mechanism**
464 A further mechanistic study to probe the potential relationship between Ca^{2+} and stiffness involved
465 perturbation of cytosolic Ca^{2+} cycling time. Elevating stimulation frequency is a recognized physiologic
466 strategy to increase diastolic Ca^{2+} levels and to apply increased cardiomyocyte workload. In response to
467 frequency elevation (2 Hz to 4 Hz) cardiomyocyte diastolic Ca^{2+} levels increased in both CTRL and HFSD (**Fig.**
468 **7A & B**) groups consistent with previous studies (Varian & Janssen, 2007; Eisner *et al.*, 2020). In the HFSD
469 cardiomyocytes this effect was markedly diminished and about half the mean magnitude of the Ca^{2+} shift
470 observed for CTRL myocytes (**Fig. 7B.** CTRL 2 Hz: 0.664±0.052, CTRL 4 Hz: 0.775±0.083, HFSD 2 Hz:
471 0.688±0.099, HFSD 4 Hz: 0.741±0.126, $F_{340:380}$, 2-way ANOVA significant interaction effect, **Fig. 7C**. CTRL
472 0.110±0.051; HFSD 0.054±0.049, $F_{340:380}$). No treatment or interaction effects were observed for systolic

473 Ca^{2+}, Ca^{2+} amplitude, or time constant of Ca^{2+} transient decay (**Table. 3**). Frequency elevation was
474 associated with a reduction in diastolic sarcomere length in both CTRL (3%) and HFSD (5%) loaded
475 cardiomyocytes (**Fig. 7D**. CTRL 2 Hz: 1.69±0.04, CTRL 4 Hz:1.64±0.05, HFSD 2 Hz: 1.69±0.04, HFSD 4 Hz:
476 1.61±0.07 µm). The combination of normal diastolic sarcomere length reduction, concomitant with
477 suppressed diastolic Ca^{2+} increase in HFSD cardiomyocytes, may indicate elevated diastolic responsiveness
478 to Ca^{2+} in the HFSD cardiomyocyte.
479
480 While frequency elevation did not change the stress/strain relation in CTRL cardiomyocytes, a significant
481 increase in the stress/strain gradient was observed with increased frequency in HFSD cardiomyocytes (**Fig.**
482 **7E&F**. CTRL 2 Hz: 0.0060±0.0056, CTRL 4 Hz:0.0068±0.0068; HFSD 2 Hz: 0.0121±0.052, HFSD 4 Hz:
483 0.0136±0.0052 (mN/mm^2) / % length). This may indicate a larger population of cross-bridges contributing to
484 diastolic stiffness at heightened workloads in HFSD cardiomyocytes although other potential non-cross-
485 bridge sources cannot be excluded. Since Ca^{2+} shift in response to increased pacing is modest (relative to
486 CTRL), increase in stiffness cannot be attributed to rise in Ca^{2+} levels *per se.* Shift in the myofilament-Ca^{2+}
487 response during diastole is a potential alternate explanation.
488
489

490 **DISCUSSION**

491

492 Here we provide the first quantitative analysis of intact cardiomyocyte stiffness and performance deficits
493 associated with acquired cardiometabolic disease. We demonstrate that a component of cardiac diastolic
494 dysfunction in cardiometabolic disease derives from intrinsic cardiomyocyte mechanical abnormality.

495

496 The concept of myocardial stiffness is a frequently invoked qualitative descriptor of the pathophysiologic
497 phenotype characterizing diastolic dysfunction. Clinically and experimentally the echocardiography
498 parameter E/e' is used as an index of myocardial stiffness in disease diagnosis. E/e' is a compound measure
499 of cellular and extracellular matrix stiffness contributors. Despite consistent *in vivo* findings, an
500 understanding of the cardiomyocyte-specific contribution to tissue stiffness has been difficult to identify.
501 Using a series of intact single cell recording maneuvers, we have established that the stiffness
502 characteristics of individual isolated cardiomyocytes from normal and dysfunctional hearts can be defined,
503 normalized and compared. Further, a significant relationship was identified between the mean stiffness of
504 single cardiomyocytes and the extent of the origin heart diastolic dysfunction (i.e. E/e' vs Young's Modulus
505 [(mN/mm2) / %length]).

506

507 To recapitulate, cardiometabolic disease induced by dietary intervention in mice was characterized by
508 marked body weight elevation (50%, 'obesity') and glucose intolerance. *In vivo* echocardiography
509 diagnosed significant diastolic dysfunction with a 35% elevation of the E/e' in HFSD animals in absence of
510 systolic functional deficit. In paced non-loaded conditions, the sarcomere contraction cycles & Ca^{2+}
511 transients (fura-2) were similar in CTRL and HFSD cardiomyocytes. When the same cardiomyocytes were
512 loaded, the shortening extent and maximal lengthening rate were reduced for both diet conditions. In HFSD
513 cardiomyocytes the reduction in deformation rate during lengthening (but not shortening) was
514 accentuated, indicating a selective negative impact of loading on relaxation of the HFSD-derived
515 cardiomyocytes. In HFSD cardiomyocytes there was a larger increase in diastolic force per cross-sectional
516 area (stress: mN/um^2) in response to standardized step increases in length (strain: % initial length [µm]).
517 From these data a 'stress/strain' parameter was determined, defining diastolic stiffness for each myocyte
518 i.e. 'Youngs Modulus' ([$mN/\mu m^2$]/[% initial length[µm]). Mean stiffness was 70% higher in cardiomyocytes
519 of HFSD animals. Thus the increase in cardiomyocyte stiffness index was approximately double the
520 elevation of the *in vivo* E/e' dysfunction index. Using matched *in vivo* and *in vitro* data, a significant
521 correlation was found between diastolic dysfunction (E/e') and mean cardiomyocyte stiffness value for
522 HFSD-diet animals, while there was no relationship between these parameters in the myocytes of CTRL-diet
523 fed group. To evaluate possible influence of mechanical state on the Ca^{2+} transient, the mean transient
524 decline parameters (tau) from non-loaded, loaded and stretched cardiomyocytes were compared. In HFSD
525 cardiomyocytes the time constant of Ca^{2+} transient decay was increased in stretched cardiomyocytes

526 relative to non-loaded, a feature not observed in CTRL cardiomyocytes. Finally, in response to an *in vitro*
527 pacing increase HFSD cardiomyocytes exhibited accentuated diastolic stiffness even with a smaller increase
528 in diastolic Ca^{2+} level. Collectively, these findings suggest a previously undescribed alteration in Ca^{2+}-
529 myofilament interactions indicative of a cross-bridge component to cardiomyocyte stiffness in
530 cardiometabolic disease.
531
532 **Dietary model of acquired metabolic syndrome and cardiac diastolic disease**
533 High fat/sugar diet feeding (i.e. 'western diet') has previously been shown experimentally to induce
534 diastolic dysfunction in rodents. Elevated E/e' is a remarkably consistent echocardiographic feature of high
535 fat/sugar diet fed mouse myocardial performance while E/A and IVRT may be elevated, reduced, or
536 unchanged relative to control counterparts (Pulinilkunnil *et al.*, 2014; Dia *et al.*, 2020; Sowers *et al.*, 2020;
537 Wingard *et al.*, 2021; Daniels *et al.*, 2022). The dietary regime employed in this study has been well
538 characterized as a model of diastolic dysfunction, with gradual development of metabolic disturbance
539 (stable rate of weight gain and mild hyperglycemia), with maintained systolic function (ejection fraction and
540 fractional shortening). The data presented here are consistent with clinical observations linking
541 cardiometabolic disease and diastolic dysfunction.
542
543 As we have reported previously, over the time span of the dietary intervention differential fibrosis is not
544 observed (Daniels *et al.*, 2022; Wells *et al.*, 2023). The finding of increased stiffness in cardiometabolic
545 disease is consistent with some aspects of prior experiments involving animal feeding of obesogenic diets,
546 using other rodent preparation types – including permeabilized cardiomyocytes, tissue strips/papillary
547 muscles, and non-paced cardiomyocytes (Leopoldo *et al.*, 2010; Gonçalves *et al.*, 2016; Sowers *et al.*, 2020).
548 Interestingly stiffness in those studies was attributed to titin or extracellular matrix properties. Our protocol
549 with intact single cardiomyocytes allows a mechanistic extension of these previous findings.
550
551 **Loading the intact cardiomyocyte - functional deficits revealed in HFSD**
552 Non-loaded contracting cardiomyocytes of CTRL and HFSD mice exhibited identical shortening-lengthening
553 cycles, but a distinctly different decrement in lengthening rate when exposed to load (i.e. auxotonic with
554 progressive 'pre-load' increase). Our findings show unequivocally that cardiomyocyte mechanical
555 dysfunction cannot be detected by analysis of non-loaded shortening. With loading, the shortening extent
556 and the maximal lengthening rates were reduced for both CTRL and HFSD. In HFSD the lengthening rate
557 reduction was accentuated even when shortening extent was accounted for. These findings indicated
558 specific influence of loading on lengthening in HFSD cardiomyocytes and could reflect impaired subcellular
559 relaxation processes specific to the HFSD myocardium.
560

561 Others have demonstrated a physiological effect of loading on shortening in cardiac cells/tissues in
562 different species (using slow pacing and sub physiologic temperature conditions), although the pronounced
563 effect on relaxation is not consistently reported (Lab *et al.*, 1984; White *et al.*, 1995; Shimkunas *et al.*,
564 2021). This is consistent with *in vivo* human clinical observations where there is a strong inverse association
565 between late-systolic loading and left ventricular wall displacement velocity during early diastole (Borlaug
566 *et al.*, 2007). Importantly, increased dependence of relaxation on after-load is reported to be an *in vivo*
567 feature of heart failure with diastolic dysfunction (Eichhorn *et al.*, 1992; Gillebert *et al.*, 2000). Regarding
568 the Ca^{2+} transient, in the current study a subtle prolongation effect is observed in both CTRL and HFSD
569 cardiomyocytes when loaded (but not stretched) which is consistent with recently reported findings in rat
570 LV trabeculae (Dowrick *et al.*, 2022). The variability in the sarcomere shortening recorded for both non-
571 loaded and loaded cardiomyocytes is notable but consistent with other studies assessing relaxation of
572 rodent cardiomyocytes (Delbridge & Roos, 1997; Clark & Campbell, 2019). A range of non-loaded
573 cardiomyocyte mean diastolic sarcomere lengths are reported in the literature. When cells are evaluated *in*
574 *vitro* and not constrained by local structural elements sarcomere lengths <1.8µm are commonly observed
575 and consistent with our findings (Lim *et al.*, 2000; Bub *et al.*, 2010). *In vitro* experimental conditions can
576 also contribute to variation in diastolic sarcomere lengths (e.g. pacing frequency, temperature and buffer
577 tonicity) (Roos *et al.*, 1982; Chung & Campbell, 2013; Khokhlova *et al.*, 2022).
578
579 **Characterizing cardiomyocyte stretch & pacing challenge responses**
580 In order to quantify intact single cardiomyocyte stiffness our approach was to apply a calibrated stretch
581 protocol, based on pre-measurement of a stretch calibration constant for each myocyte, tracking changes
582 in force generation and cytosolic Ca^{2+} responses for each stretch step. This calibrated step-by-step
583 approach enabled the stress and strain data to be gathered from actively paced cardiomyocytes over
584 extended periods (i.e. 80-100 sec) and computed to generate a definitive, comparative stiffness parameter
585 for each cardiomyocyte.
586
587 In the intact myocyte model, the internal cytosolic regulatory milieu is preserved, and the
588 cytoskeletal/sarcomeric/organelle structural framework is integral. Thus contributions to diastolic
589 'stiffness' reflect components of the structural passive resistance to deformation and the basal crossbridge-
590 derived activity. Recent studies of permeabilized cardiac muscle strip bundles have explored the separate
591 contributions of mictrotubule, titin, actin-associated, sarcolemmal and desmin-linked components to
592 passive force development (Loescher *et al.*, 2023). Prior studies of 'skinned' or quiescent myocardial
593 preparations have also identified sources of passive stiffness elevation, with titin isoform switch and
594 modification identified as major modulators of stiffness in cardiometabolic disease (Leopoldo *et al.*, 2010;
595 Hamdani *et al.*, 2013; Gonçalves *et al.*, 2016; Hopf *et al.*, 2018; Sowers *et al.*, 2020; Abdellatif *et al.*, 2021).
596

597 Our findings indicate involvement of a cytosolic Ca^{2+} component of the stretch response. Ca^{2+} fluorescence
598 analyses from these stretch protocols showed novel stretch-dependent prolongation of Ca^{2+} transient
599 decay in the HFSD cardiomyocytes. The time constant of Ca^{2+} transient decay increased with loading and
600 further with stretching – a feature not evident in CTRL cardiomyocytes and which provides additional
601 mechanistic insight .
602
603 The final pacing frequency protocol was implemented as a relative workload stress to the loaded
604 cardiomyocyte. With a doubling of pacing frequency, a significant increase in the stress/strain gradient was
605 observed in HFSD cardiomyocytes (and not CTRL), and a similar reduction in diastolic sarcomere length in
606 both CTRL and HFSD was observed. While cardiomyocyte diastolic Ca^{2+} level increased in both CTRL and
607 HFSD – the HFSD increase was less marked than CTRL. This was a surprising finding, not previously
608 reported in any other model setting. A suggestion of Ca^{2+} hyper-sensitivity arises (Davis *et al.*, 2007)
609 amongst other explanations to consider.
610
611 **Mechanistic insights into cross-bridge derived stiffness**
612 Here we report that a cardiometabolic disease phenotype induced by obesogenic diet includes a 70%
613 increase in cardiomyocyte stiffness which contributes to a 35% increase in diastolic dysfunction *in vivo* (by
614 echo E/e'). Several lines of evidence emerging from this study suggest that Ca^{2+} -related mechanism/s may
615 contribute to cardiomyocyte stiffness increase. Specifically, in the loaded HFSD cardiomyocyte (vs CTRL):
616 a) load confers accentuated lengthening rate deficit
617 b) with stretch, the Ca^{2+} transient decay time course is prolonged
618 c) with more rapid pacing, relatively small increases in diastolic Ca^{2+} are associated with elevated stiffness
619 Together these cardiomyocyte phenotypes would be consistent with selective impairment of relaxation
620 rate, selective myofilament hyper-activation, impeded diastolic filling and reduced diastolic reserve.
621
622 This combination of observations is consistent with the notion that stretch-dependent cross-bridge
623 attachment is prolonged in HFSD cardiomyocytes (or conversely detachment is delayed). We can speculate
624 that an alteration in the 3-dimensional geometry of the low affinity Ca^{2+} binding pocket in troponin C (TnC)
625 would produce this effect, by stabilizing Ca^{2+} in the pocket for longer every activation cycle. This could
626 increase TnC buffering power which would explain the relatively small Ca^{2+} rise in HFSD in response to
627 increased pacing (Eisner *et al.*, 2023). A manifestation of this altered binding function could be apparent
628 Ca^{2+} hypersensitivity. The TnC-Ca^{2+} dissociation rate has been theorized as an effector of the transient
629 decay time-course (Robinson *et al.*, 2018). A role for the troponin complex in regulation of Ca^{2+} affinity is
630 well established (Chemla *et al.*, 2000). Given the load and stretch-dependent nature of these findings, a
631 role for stress sensor proteins such as titin is likely. Indeed, there is some evidence to suggest that titin
632 isoform regulates TnC low-affinity binding pocket opening and Ca^{2+} affinity in response to stretch via

633 regulating the number of attached cross-bridges (Li *et al.*, 2019). Further evidence of structural
634 modifications of specific myofilament regions which form and regulate this pocket is required. Mass
635 spectrometry studies by us and others provide proof of concept of relevant post-translational modification
636 types (Janssens *et al.*, 2018; Loescher *et al.*, 2022).
637
638 **Limitations**
639 Given the diastolic dysfunction focus of this study, investigations have primarily examined cardiomyocyte
640 relaxation and lengthening behaviors. Diastolic and systolic interactions are important and additional
641 protocols are in development for these studies. In this regard, we defer to the extensive body of
642 technologic research undertaken to develop software and instrumentation to perform single
643 cardiomyocyte 'Pressure-Volume (PV) loops' (Helmes *et al.*, 2016). Using this approach, to mimic PV cycles
644 in the intact myocardium, stretch is applied after relaxation has occurred by using a force clamp to
645 maintain a predefined diastolic force level. This approach has been used to discover that titin truncation
646 shifts the working sarcomere length range preserving diastolic stiffness at the expense of systolic
647 performance (Methawasin *et al.*, 2022) and that highly compliant titin allows cardiomyocytes to function at
648 high diastolic Ca^{2+} levels (Najafi *et al.*, 2019). Potentially, this approach could also be used to evaluate the
649 temporal relationship between slow or incomplete relaxation and cardiomyocyte cross-bridge derived
650 stiffness in a semi-situ manner. Operator expertise is imperative with this system which to date has been
651 very productive in the hands of the developers.
652
653 In our work we have adopted a pragmatic approach, simpler to implement – although still very challenging.
654 Our protocol involves the application of cumulative ramp steps with about 20% non-loaded-to-loaded
655 myocyte conversion success rate. When animals have many months of dietary treatment history, and as
656 cell isolation from older and diseased hearts is difficult, an optimized loading and stretching approach is
657 key. The two approaches have not been benchmarked, although it can be predicted that the viscous
658 components of stiffness are likely underestimated when stretches are slow and relatively small such as in
659 the current study (Caporizzo & Prosser, 2021). The capacity to directly and reproducibly determine Young's
660 Modulus (stress/strain) with a slow stretch routine has useful comparative value. An additional aspect of
661 our pragmatic approach has been to evaluate cardiomyocyte segment stretches as average sarcomere
662 stretch methods can be challenging to track optically.
663
664 With ongoing research, a priority is to undertake longitudinal studies, including both sexes, to investigate
665 the relative timing of the emergence of *in vivo* and *in vitro* stiffness phenotypes as differences in Ca^{2+}
666 handling have previously been observed between control male and female rodents (Farrell *et al.*, 2010).
667 This has high translational relevance as we have previously identified a differential time course of diastolic

668 dysfunction emergence in females and males, with increased female vulnerability (Reichelt *et al.*, 2013;
669 Chandramouli *et al.*, 2018).
670
671 **In conclusion**
672 This is the first study to link elevated intact single cardiomyocyte stiffness with *in vivo* diastolic dysfunction
673 in a dietary acquired cardiometabolic disease mouse model. The novel findings identify augmented load
674 dependent TnC-Ca^{2+} interactions as one potential feature of myofilament function which contributes to
675 cardiomyocyte stiffness in hearts exhibiting cardiometabolic diastolic dysfunction. Taken together, the
676 findings emphasize the importance of mechanical loading and pacing frequency in revealing latent diastolic
677 abnormalities at the cardiomyocyte level. The rationale for further studies identifying specific subcellular
678 and molecular mechanisms of cardiomyocyte stiffness in cardiometabolic disease prior to failure onset is
679 compelling.
680
681 **BIOGRAPHY**

682
683 **Johannes Janssens** completed his PhD in the Department of Anatomy and Physiology at the University of
684 Melbourne (Australia) where the current work was performed. After completing his PhD he received a
685 Fulbright Postdoctoral Scholarship to develop a novel blood biomarker of diabetic heart disease at Cedars-
686 Sinai Medical Center (Los Angeles, CA) where he continues to work currently. Johannes' research
687 aspirations involve linking large-scale proteomic features of hearts and cardiomyocytes with their
688 functional phenotype to develop novel therapeutic and diagnostic strategies for cardiac pathophysiology. In
689 particular diseases where diastolic dysfunction is a prominent characteristic.
690
691 **ADDITIONAL INFORMATION**
692
693 **Data availability statement**
694 The data that support the findings of this study are available from the corresponding author upon
695 reasonable request.
696

697 **Competing interests**

698 The authors declare that they have no competing interests.

699

700 **Author contributions**

701 All experiments were performed at the Cardiac Phenomics Laboratory at the University of Melbourne,
702 Australia. J.V.J., K.M.M. and L.M.D.D. contributed to the conception and research design of the work. All
703 authors contributed to the acquisition, analysis or interpretation of data for the work and contributed to
704 drafting the work or revising it critically for important intellectual content. All authors provide final
705 approval of the version to be published and agreement to be accountable for all aspects of the work.

706

707 **Funding**

708 This work was supported by grants from the National Health and Medical Research Council of Australia
709 (LMDD: NHMRCA 1157320), the Diabetes Australia Research Trust (LMDD), the National Heart Foundation
710 of Australia (LMDD: NHFA), the New Zealand Marsden Fund (KMM: 19-UOA-268), the Health Research
711 Council of New Zealand (KMM:19/190), and the National Institutes of Health USA (JVE: R01 HL155346-01 &
712 R01 HL144509-01).

713

714

715 **REFERENCES**

716 Abdellatif M et al. (2021). Nicotinamide for the treatment of heart failure with preserved ejection fraction.
717 *Sci Transl Med* **13,** eabd7064.

718 Aurigemma GP, Zile MR & Gaasch WH (2006). Contractile Behavior of the Left Ventricle in Diastolic Heart
719 Failure. *Circulation* **113,** 296–304.

720 Bollensdorff C, Lookin O & Kohl P (2011). Assessment of contractility in intact ventricular cardiomyocytes
721 using the dimensionless "Frank-Starling Gain" index. *Pflugers Arch* **462,** 39–48.

722 Borlaug BA, Melenovsky V, Redfield MM, Kessler K, Chang H-J, Abraham TP & Kass DA (2007). Impact of
723 Arterial Load and Loading Sequence on Left Ventricular Tissue Velocities in Humans. *Journal of the*
724 *American College of Cardiology* **50,** 1570–1577.

725 Bub G, Camelliti P, Bollensdorff C, Stuckey DJ, Picton G, Burton RAB, Clarke K & Kohl P (2010). Measurement
726 and analysis of sarcomere length in rat cardiomyocytes in situ and in vitro. *Am J Physiol Heart Circ*
727 *Physiol* **298,** H1616–H1625.

728 Caporizzo MA & Prosser BL (2021). Need for Speed: The Importance of Physiological Strain Rates in
729 Determining Myocardial Stiffness. *Front Physiol* **12,** 696694.

730 Chandramouli C, Reichelt ME, Curl CL, Varma U, Bienvenu LA, Koutsifeli P, Raaijmakers AJA, De Blasio MJ,
731 Qin CX, Jenkins AJ, Ritchie RH, Mellor KM & Delbridge LMD (2018). Diastolic dysfunction is more
732 apparent in STZ-induced diabetic female mice, despite less pronounced hyperglycemia. *Sci Rep* **8,**
733 2346.

734 Chemla D, Coirault C, Hébert J-L & Lecarpentier Y (2000). Mechanics of Relaxation of the Human Heart.
735 *Physiology* **15,** 78–83.

736 Chung CS & Campbell KS (2013). Temperature and transmural region influence functional measurements in
737 unloaded left ventricular cardiomyocytes. *Physiol Rep* **1,** e00158.

738 Clark JA & Campbell SG (2019). Diverse relaxation rates exist among rat cardiomyocytes isolated from a
739 single myocardial region. *J Physiol* **597,** 711–722.

740 Curl CL, Danes VR, Bell JR, Raaijmakers AJA, Ip WTK, Chandramouli C, Harding TW, Porrello ER, Erickson JR,
741 Charchar FJ, Kompa AR, Edgley AJ, Crossman DJ, Soeller C, Mellor KM, Kalman JM, Harrap SB &
742 Delbridge LMD (2018). Cardiomyocyte Functional Etiology in Heart Failure With Preserved Ejection
743 Fraction Is Distinctive-A New Preclinical Model. *J Am Heart Assoc* **7,** e007451.

744 Daniels LJ, Macindoe C, Koutsifeli P, Annandale M, Raaijmakers AJA, Weeks KL, Bell JR, Janssens JV, Curl CL,
745 Delbridge LMD & Mellor KM (2022). Myocardial deformation imaging by 2D speckle tracking
746 echocardiography for assessment of diastolic dysfunction in murine cardiopathology.
747 2022.08.06.503061. Available at: https://www.biorxiv.org/content/10.1101/2022.08.06.503061v1
748 [Accessed May 22, 2023].

749 Davis J, Wen H, Edwards T & Metzger JM (2007). Thin Filament Disinhibition by Restrictive Cardiomyopathy
750 Mutant R193H Troponin I Induces Ca2+-Independent Mechanical Tone and Acute Myocyte
751 Remodeling. *Circulation Research* **100,** 1494–1502.

752 Delbridge LM & Roos KP (1997). Optical methods to evaluate the contractile function of unloaded isolated
753 cardiac myocytes. *J Mol Cell Cardiol* **29,** 11–25.

754 Delbridge LMD, Bell JR, Weeks KL, Raaijmakers AJA & Mellor KM (2022). HFpEF etiology - Can focus on sex-
755 specific mechanisms deliver insights for all? *J Mol Cell Cardiol* **173,** 71–72.

Dia M, Gomez L, Thibault H, Tessier N, Leon C, Chouabe C, Ducreux S, Gallo-Bona N, Tubbs E, Bendridi N, Chanon S, Leray A, Belmudes L, Couté Y, Kurdi M, Ovize M, Rieusset J & Paillard M (2020). Reduced reticulum–mitochondria Ca2+ transfer is an early and reversible trigger of mitochondrial dysfunctions in diabetic cardiomyopathy. *Basic Res Cardiol* **115,** 74.

Dowrick JM, Tran K, Garrett AS, Anderson AJ, Nielsen PMF, Taberner AJ & Han J-C (2022). Work-loop contractions reveal that the afterload-dependent time course of cardiac Ca2+ transients is modulated by preload. *Journal of Applied Physiology* **133,** 663–675.

Eichhorn EJ, Willard JE, Alvarez L, Kim AS, Glamann DB, Risser RC & Grayburn PA (1992). Are contraction and relaxation coupled in patients with and without congestive heart failure? *Circulation* **85,** 2132–2139.

Eisner D, Neher E, Taschenberger H & Smith G (2023). Physiology of intracellular calcium buffering. *Physiological Reviews* **103,** 2767–2845.

Eisner DA, Caldwell JL, Trafford AW & Hutchings DC (2020). The Control of Diastolic Calcium in the Heart. *Circ Res* **126,** 395–412.

Fabiato A & Fabiato F (1978). Myofilament-generated tension oscillations during partial calcium activation and activation dependence of the sarcomere length-tension relation of skinned cardiac cells. *J Gen Physiol* **72,** 667–699.

Farrell SR, Ross JL & Howlett SE (2010). Sex differences in mechanisms of cardiac excitation-contraction coupling in rat ventricular myocytes. *Am J Physiol Heart Circ Physiol* **299,** H36-45.

Fowler ED, Benoist D, Drinkhill MJ, Stones R, Helmes M, Wüst RCI, Stienen GJM, Steele DS & White E (2015). Decreased creatine kinase is linked to diastolic dysfunction in rats with right heart failure induced by pulmonary artery hypertension. *J Mol Cell Cardiol* **86,** 1–8.

Gillebert TC, Leite-Moreira AF & De Hert SG (2000). Load dependent diastolic dysfunction in heart failure. *Heart Fail Rev* **5,** 345–355.

Gonçalves N, Silva AF, Rodrigues PG, Correia E, Moura C, Eloy C, Roncon-Albuquerque R, Falcão-Pires I & Leite-Moreira AF (2016). Early cardiac changes induced by a hypercaloric Western-type diet in "subclinical" obesity. *American Journal of Physiology-Heart and Circulatory Physiology* **310,** H655–H666.

Grundy D (2015). Principles and standards for reporting animal experiments in The Journal of Physiology and Experimental Physiology. *J Physiol* **593,** 2547–2549.

Hamdani N, Franssen C, Lourenço A, Falcão-Pires I, Fontoura D, Leite S, Plettig L, López B, Ottenheijm CA, Becher PM, González A, Tschöpe C, Díez J, Linke WA, Leite-Moreira AF & Paulus WJ (2013). Myocardial Titin Hypophosphorylation Importantly Contributes to Heart Failure With Preserved Ejection Fraction in a Rat Metabolic Risk Model. *Circulation: Heart Failure* **6,** 1239–1249.

Heather LC, Hafstad AD, Halade GV, Harmancey R, Mellor KM, Mishra PK, Mulvihill EE, Nabben M, Nakamura M, Rider OJ, Ruiz M, Wende AR & Ussher JR (2022). Guidelines on models of diabetic heart disease. *Am J Physiol Heart Circ Physiol* **323,** H176–H200.

Helmes M, Najafi A, Palmer BM, Breel E, Rijnveld N, Iannuzzi D & van der Velden J (2016). Mimicking the cardiac cycle in intact cardiomyocytes using diastolic and systolic force clamps; measuring power output. *Cardiovasc Res* **111,** 66–73.

Hopf A-E, Andresen C, Kötter S, Isić M, Ulrich K, Sahin S, Bongardt S, Röll W, Drove F, Scheerer N, Vandekerckhove L, De Keulenaer GW, Hamdani N, Linke WA & Krüger M (2018). Diabetes-Induced Cardiomyocyte Passive Stiffening Is Caused by Impaired Insulin-Dependent Titin Modification and Can Be Modulated by Neuregulin-1. *Circulation Research* **123,** 342–355.

Howlett SE, Grandy SA & Ferrier GR (2006). Calcium spark properties in ventricular myocytes are altered in aged mice. *American Journal of Physiology-Heart and Circulatory Physiology* **290,** H1566–H1574.

Jackson AM et al. (2022). Diabetes and pre-diabetes in patients with heart failure and preserved ejection fraction. *Eur J Heart Fail* **24,** 497–509.

Janssens JV, Ma B, Brimble MA, Van Eyk JE, Delbridge LMD & Mellor KM (2018). Cardiac troponins may be irreversibly modified by glycation: novel potential mechanisms of cardiac performance modulation. *Sci Rep* **8,** 16084.

Janssens JV, Raaijmakers AJA, Weeks KL, Bell JR, Mellor KM, Curl CL & Delbridge LMD (2024). The cardiomyocyte origins of diastolic dysfunction: cellular components of myocardial stiffness. *Am J Physiol Heart Circ Physiol*; DOI: 10.1152/ajpheart.00334.2023.

Kamon T, Kaneko H, Itoh H, Kiriyama H, Koyama K, Fujiu K, Morita H, Uno K, Hayashi N & Komuro I (2020). Association between insulin resistance and left ventricular diastolic dysfunction in non-diabetic general population. *European Heart Journal* **41,** ehaa946.3057.

Khokhlova A, Myachina T, Volzhaninov D, Butova X, Kochurova A, Berg V, Gette I, Moroz G, Klinova S, Minigalieva I, Solovyova O, Danilova I, Sokolova K, Kopylova G & Shchepkin D (2022). Type 1 Diabetes Impairs Cardiomyocyte Contractility in the Left and Right Ventricular Free Walls but Preserves It in the Interventricular Septum. *Int J Mol Sci* **23,** 1719.

Kilfoil PJ, Lotteau S, Zhang R, Yue X, Aynaszyan S, Solymani RE, Cingolani E, Marbán E & Goldhaber JI (2020). Distinct features of calcium handling and β-adrenergic sensitivity in heart failure with preserved versus reduced ejection fraction. *J Physiol* **598,** 5091–5108.

Kittleson MM, Panjrath GS, Amancherla K, Davis LL, Deswal A, Dixon DL, Januzzi JL & Yancy CW (2023). 2023 ACC Expert Consensus Decision Pathway on Management of Heart Failure With Preserved Ejection Fraction: A Report of the American College of Cardiology Solution Set Oversight Committee. *Journal of the American College of Cardiology* **81,** 1835–1878.

Lab MJ, Allen DG & Orchard CH (1984). The effects of shortening on myoplasmic calcium concentration and on the action potential in mammalian ventricular muscle. *Circulation Research* **55,** 825–829.

Lam CSP, Arnott C, Beale AL, Chandramouli C, Hilfiker-Kleiner D, Kaye DM, Ky B, Santema BT, Sliwa K & Voors AA (2019). Sex differences in heart failure. *European Heart Journal* **40,** 3859–3868c.

Leopoldo AS, Sugizaki MM, Lima-Leopoldo AP, do Nascimento AF, de Azevedo Melo Luvizotto R, de Campos DHS, Okoshi K, Pai-Silva MD, Padovani CR & Cicogna AC (2010). Cardiac remodeling in a rat model of diet-induced obesity. *Can J Cardiol* **26,** 423–429.

Leung M, Phan V, Whatmough M, Heritier S, Wong VW & Leung DY (2015). Left ventricular diastolic reserve in patients with type 2 diabetes mellitus. *Open Heart* **2,** e000214.

Li K-L, Methawasin M, Tanner BCW, Granzier HL, Solaro RJ & Dong W-J (2019). Sarcomere length–dependent effects on Ca2+-troponin regulation in myocardium expressing compliant titin. *J Gen Physiol* **151,** 30–41.

836 Lim CC, Apstein CS, Colucci WS & Liao R (2000). Impaired Cell Shortening and Relengthening with Increased
837 Pacing Frequency are Intrinsic to the Senescent Mouse Cardiomyocyte. *Journal of Molecular and*
838 *Cellular Cardiology* **32,** 2075–2082.

839 Llano-Diez M, Sinclair J, Yamada T, Zong M, Fauconnier J, Zhang S-J, Katz A, Jardemark K, Westerblad H,
840 Andersson DC & Lanner JT (2016). The Role of Reactive Oxygen Species in β-Adrenergic Signaling in
841 Cardiomyocytes from Mice with the Metabolic Syndrome. *PLoS One* **11,** e0167090.

842 Lo Q & Thomas L (2010). Echocardiographic evaluation of diastolic heart failure. *Australas J Ultrasound Med*
843 **13,** 14–26.

844 Loescher CM, Freundt JK, Unger A, Hessel AL, Kühn M, Koser F & Linke WA (2023). Titin governs myocardial
845 passive stiffness with major support from microtubules and actin and the extracellular matrix. *Nat*
846 *Cardiovasc Res* **2,** 991–1002.

847 Loescher CM, Hobbach AJ & Linke WA (2022). Titin (TTN): from molecule to modifications, mechanics, and
848 medical significance. *Cardiovascular Research* **118,** 2903–2918.

849 Louch WE (2020). A horse of a different colour: distinct mechanisms of HFpEF and HFrEF. *J Physiol* **598,**
850 5005–5006.

851 McHugh K, DeVore AD, Wu J, Matsouaka RA, Fonarow GC, Heidenreich PA, Yancy CW, Green JB, Altman N
852 & Hernandez AF (2019). Heart Failure With Preserved Ejection Fraction and Diabetes: JACC State-
853 of-the-Art Review. *J Am Coll Cardiol* **73,** 602–611.

854 Mellor KM, Bell JR, Young MJ, Ritchie RH & Delbridge LMD (2011). Myocardial autophagy activation and
855 suppressed survival signaling is associated with insulin resistance in fructose-fed mice. *Journal of*
856 *Molecular and Cellular Cardiology* **50,** 1035–1043.

857 Mellor KM, Wendt IR, Ritchie RH & Delbridge LMD (2012). Fructose diet treatment in mice induces
858 fundamental disturbance of cardiomyocyte Ca2+ handling and myofilament responsiveness. *Am J*
859 *Physiol Heart Circ Physiol* **302,** H964-972.

860 Methawasin M, Farman GP, Granzier-Nakajima S, Strom J, Kiss B, Smith JE & Granzier H (2022). Shortening
861 the thick filament by partial deletion of titin's C-zone alters cardiac function by reducing the
862 operating sarcomere length range. *J Mol Cell Cardiol* **165,** 103–114.

863 Mirsky I (1976). Assessment of passive elastic stiffness of cardiac muscle: mathematical concepts,
864 physiologic and clinical considerations, directions of future research. *Prog Cardiovasc Dis* **18,** 277–
865 308.

866 Najafi A, van de Locht M, Schuldt M, Schönleitner P, van Willigenburg M, Bollen I, Goebel M, Ottenheijm
867 CAC, van der Velden J, Helmes M & Kuster DWD (2019). End-diastolic force pre-activates
868 cardiomyocytes and determines contractile force: role of titin and calcium. *J Physiol* **597,** 4521–
869 4531.

870 Najafi A, Sequeira V, Helmes M, Bollen IAE, Goebel M, Regan JA, Carrier L, Kuster DWD & Van Der Velden J
871 (2016). Selective phosphorylation of PKA targets after β-adrenergic receptor stimulation impairs
872 myofilament function in Mybpc3-targeted HCM mouse model. *Cardiovasc Res* **110,** 200–214.

873 Natali AJ, Turner DL, Harrison SM & White E (2001). Regional effects of voluntary exercise on cell size and
874 contraction-frequency responses in rat cardiac myocytes. *Journal of Experimental Biology* **204,**
875 1191–1199.

876 Patil VC, Patil HV, Shah KB, Vasani JD & Shetty P (2011). Diastolic dysfunction in asymptomatic type 2
877 diabetes mellitus with normal systolic function. *J Cardiovasc Dis Res* **2,** 213–222.

878 Peyronnet R, Bollensdorff C, Capel RA, Rog-Zielinska EA, Woods CE, Charo DN, Lookin O, Fajardo G, Ho M,
879 Quertermous T, Ashley EA & Kohl P (2017). Load-dependent effects of apelin on murine
880 cardiomyocytes. *Prog Biophys Mol Biol* **130,** 333–343.

881 Pulinilkunnil T, Kienesberger PC, Nagendran J, Sharma N, Young ME & Dyck JRB (2014). Cardiac-specific
882 adipose triglyceride lipase overexpression protects from cardiac steatosis and dilated
883 cardiomyopathy following diet-induced obesity. *Int J Obes* **38,** 205–215.

884 Redfield MM (2016). Heart Failure with Preserved Ejection Fraction. *N Engl J Med* **375,** 1868–1877.

885 Reichelt ME, Mellor KM, Bell JR, Chandramouli C, Headrick JP & Delbridge LMD (2013). Sex, sex steroids,
886 and diabetic cardiomyopathy: making the case for experimental focus. *Am J Physiol Heart Circ*
887 *Physiol* **305,** H779-792.

888 Robinson P, Liu X, Sparrow A, Patel S, Zhang Y-H, Casadei B, Watkins H & Redwood C (2018). Hypertrophic
889 cardiomyopathy mutations increase myofilament Ca2+ buffering, alter intracellular Ca2+ handling,
890 and stimulate Ca2+-dependent signaling. *J Biol Chem* **293,** 10487–10499.

891 Roos KP, Brady AJ & Tan ST (1982). Direct measurement of sarcomere length from isolated cardiac cells.
892 *American Journal of Physiology-Heart and Circulatory Physiology* **242,** H68–H78.

893 Rozenbaum Z, Topilsky Y, Khoury S, Pereg D & Laufer-Perl M (2019). Association of body mass index and
894 diastolic function in metabolically healthy obese with preserved ejection fraction. *Int J Cardiol* **277,**
895 147–152.

896 Saad NS, Mashali MA, Repas SJ & Janssen PML (2023). Altering Calcium Sensitivity in Heart Failure: A
897 Crossroads of Disease Etiology and Therapeutic Innovation. *Int J Mol Sci* **24,** 17577.

898 Satoh H, Delbridge LM, Blatter LA & Bers DM (1996). Surface:volume relationship in cardiac myocytes
899 studied with confocal microscopy and membrane capacitance measurements: species-dependence
900 and developmental effects. *Biophys J* **70,** 1494–1504.

901 Shimkunas R et al. (2021). Mechanical Load Regulates Excitation-Ca2+ Signaling-Contraction in
902 Cardiomyocyte. *Circ Res* **128,** 772–774.

903 Sotomi Y et al. (2021). Sex Differences in Heart Failure With Preserved Ejection Fraction. *J Am Heart Assoc*
904 **10,** e018574.

905 Sowers JR, Habibi J, Jia G, Bostick B, Manrique-Acevedo C, Lastra G, Yang Y, Chen D, Sun Z, Domeier TL,
906 Durante W, Whaley-Connell AT, Hill MA, Jaisser F, DeMarco VG & Aroor AR (2020). Endothelial
907 sodium channel activation promotes cardiac stiffness and diastolic dysfunction in Western diet fed
908 female mice. *Metabolism* **109,** 154223.

909 Varian KD & Janssen PML (2007). Frequency-dependent acceleration of relaxation involves decreased
910 myofilament calcium sensitivity. *American Journal of Physiology-Heart and Circulatory Physiology*
911 **292,** H2212–H2219.

912 Villalobos Lizardi JC, Baranger J, Nguyen MB, Asnacios A, Malik A, Lumens J, Mertens L, Friedberg MK,
913 Simmons CA, Pernot M & Villemain O (2022). A guide for assessment of myocardial stiffness in
914 health and disease. *Nat Cardiovasc Res* **1,** 8–22.

915 Wang Q, Wang Y, West TM, Liu Y, Reddy GR, Barbagallo F, Xu B, Shi Q, Deng B, Wei W & Xiang YK (2020).
916 Carvedilol induces biased β1 adrenergic receptor-Nitric oxide synthase 3-cyclic guanylyl
917 monophosphate signaling to promote cardiac contractility. *Cardiovasc Res*cvaa266.

918 Wells SP, Raaijmakers AJA, Curl CL, O'Shea C, Hayes S, Mellor KM, Kalman JM, Kirchhof P, Pavlovic D,
919 Delbridge LMD & Bell JR (2023). Localized cardiomyocyte lipid accumulation is associated with
920 slowed epicardial conduction in rats. *J Gen Physiol* **155,** e202213296.

921 West TM, Wang Q, Deng B, Zhang Y, Barbagallo F, Reddy GR, Chen D, Phan KS, Xu B, Isidori A & Xiang YK
922 (2019). Phosphodiesterase 5 Associates With β2 Adrenergic Receptor to Modulate Cardiac Function
923 in Type 2 Diabetic Hearts. *JAHA*; DOI: 10.1161/JAHA.119.012273.

924 White E, Boyett MR & Orchard CH (1995). The effects of mechanical loading and changes of length on single
925 guinea-pig ventricular myocytes. *The Journal of Physiology* **482,** 93–107.

926 Wingard MC, Dalal S, Shook PL, Myers R, Connelly BA, Thewke DP, Singh M & Singh K (2021). Deficiency of
927 ataxia-telangiectasia mutated kinase modulates functional and biochemical parameters of the
928 heart in response to Western-type diet. *Am J Physiol Heart Circ Physiol* **320,** H2324–H2338.

929 Zhou P & Pu WT (2016). Recounting Cardiac Cellular Composition. *Circulation Research* **118,** 368–370.

930

931 **FIGURE LEGENDS**

932 **Fig.1 Systemic indicators of cardiometabolic disease and *in vivo* diastolic function in high-fat/sugar diet**
933 **(HFSD) vs control (CTRL) mice.**
934 **A.** Body weight elevation at 5 week intervals up to 30 weeks of dietary treatment (last timepoint full cohort
935 intact. N = 16 – 17 mice per group).
936 **B.** Glucose tolerance testing at 23-24 weeks post dietary intervention; N = 6 mice per group).
937 **C.** Echocardiography exemplar blood flow and tissue doppler images from which diastolic indices were
938 derived for CTRL and HFSD mice. Panels with orange outline: HFSD mitral blood flow & annular wall motion.
939 Panels with blue outline: CTRL mitral blood flow & annular wall motion. (N = 14-16 mice per group)
940 **D.** Early diastolic mitral annular blood flow (E) was increased in HFSD.
941 **E.** Early diastolic mitral annular wall velocity (e') was decreased in HFSD.
942 **F.** Deceleration time of early diastolic mitral annular blood flow was decreased in HFSD.
943 **G.** Ratio of early diastolic blood flow to wall velocity (E/e') was increased in HFSD.
944
945 Time-course data analysed using two-way repeated measures ANOVA with Sidak post-hoc test with p-value
946 for 'time x diet' effect presented. Comparisons between two treatment groups performed using student's
947 t-test. Data presented as mean ± standard deviation.
948
949
950 **Fig.2 Non-loaded sarcomere and Ca^{2+} dynamics in CTRL and HFSD cardiomyocytes.**
951 **A.** Mean sarcomere contraction cycles presented as a percentage of diastolic sarcomere length for CTRL
952 and HFSD cardiomyocytes
953 **B-C.** Mean diastolic sarcomere length and extent of sarcomere shortening for CTRL and HFSD
954 cardiomyocytes.
955 **D.** Mean sarcomere shortening and lengthening rate records (time derivative of sarcomere contraction-
956 relaxation cycle) for CTRL and HFSD cardiomyocytes. The nadir and zenith represent maximal shortening
957 and lengthening rates respectively.
958 **E-F.** Maximal rate of lengthening and shortening rates for CTRL and HFSD cardiomyocytes.
959 **G.** Mean Ca^{2+} transient records for CTRL and HFSD cardiomyocytes.
960 **H-J.** Mean Ca^{2+} levels (systolic and diastolic) and time constant of transient decay (*tau*) in HFSD and CTRL
961 cardiomyocytes.
962
963 Mean data computed from average of 20 cycles per cardiomyocyte to derive group mean (N = 6-8 mice per
964 group, n = 32-49 cells per group). Comparisons between two treatment groups performed using student's
965 t-test (all $p>0.05$, ns). Data presented as mean ± standard deviation.
966

Fig. 3 Sarcomere shortening and lengthening in non-loaded and loaded pacing states.
A. Exemplar non-loaded and loaded sarcomere contraction cycles for the same cardiomyocyte (CTRL).
B-C. Extent of sarcomere shortening and maximum rate of lengthening, measured for each cardiomyocyte in non-loaded and loaded state for CTRL and HFSD groups combined (N = 9 mice, n = 25 cells). Mean data for CTRL and HFSD are presented as grey points to the left (non-loaded) and right (loaded) of individual cardiomyocyte data.
D. Correlation of loading associated sarcomere shortening change and maximum rate of lengthening change for CTRL and HFSD combined.
E. Mean loading effect on maximum deformation rate during lengthening ((µm/s) / µm; maximum rate of lengthening (µm/s) normalized by shortening extent (µm)) for CTRL vs HFSD. (CTRL: N = 5 mice, n = 14 cells; HFSD: N = 4 mice, n = 12 cells). Significant ANOVA interaction effect (diet treatment x load state).
F. Mean decrement in deformation rate during lengthening ((µm/s) / µm).

Comparison of cardiomyocyte responses in different loading conditions analysed by paired t-test. Comparison of cardiomyocytes from different treatment groups analysed by unpaired t-test. A 2-way ANOVA with repeated measures used for analysis of two independent variables. Data fitted with linear regression model and calculation of Pearson's correlation coefficient. Data presented as mean ± standard deviation.

Fig. 4. Cardiomyocyte standardized stretch protocol.
A. Image of a left ventricular cardiomyocyte longitudinally attached to glass rods. Edge-tracking used to measure inter-rod distance (marked as blue bars) for cardiomyocyte segment analyses. The delineated region of interest (marked pink) represents the area from which Fast Fourier Transform analysis of sarcomere striations was performed to derive sarcomere-specific data.
B. Exemplar traces depict the change in glass rod internal distance in response to successive 0.5V piezo motor inputs used for calibration of stretch protocol for each individual cardiomyocyte to allow normalized comparisons.
C. Measuring stress and strain during progressive cardiomyocyte stretch. Exemplar force, sarcomere length and rod edge-tracker traces during the first stretch of a stress-length protocol.
D. Comparison of variability of cell stretches performed using a uniform (preset) stretch constant and the individually derived stretch calibration constant. Strain was measured as the %change in segment length relative to the initial segment length. Reproducibility is optimized using the individual stretch calibration constant. Data shown as median ± interquartile range.

1002 **Fig. 5 Quantifying diastolic stiffness in CTRL vs HFSD cardiomyocytes using strain normalization methods**
1003 **A.** Exemplar stress recordings of CTRL and HFSD cardiomyocytes undergoing 'stress-length' protocol (2Hz
1004 paced). Diastolic baseline stress shifts indicated by broken line.
1005 **B.** Diastolic (pair of lower lines) and systolic (pair of upper lines) sarcomere mean stress- sarcomere length
1006 (SL) relations in CTRL cardiomyocytes (N = 5 mice, n = 9 cells).
1007 **C.** Diastolic mean stress-sarcomere length relation (linear regression fit) for HFSD and CTRL.
1008 **D.** Diastolic stress (mN/mm^2) normalized relative to sarcomere stretch (µm) yields sarcomere stress/strain =
1009 stiffness [(mN/mm^2) /strain (µm)] for HFSD and CTRL.
1010 **E.** Diastolic mean cardiomyocyte segment stress-length relation (linear regression fit) for HFSD and CTRL.
1011 **F.** Diastolic stress (mN/mm^2) normalized relative to segment stretch (% length) yields cardiomyocyte
1012 segment stress/strain = stiffness [(mN/mm^2) /strain (% length)] for HFSD & CTRL.
1013 **G.** Correlation (linear regression fit) of *in vitro* cardiomyocyte segment diastolic stiffness (stress/strain) with
1014 *in vivo* diastolic dysfunction E/e' (blood flow/wall motion) in CTRL and HFSD. Cardiomyocyte data averaged
1015 per heart.
1016
1017 Comparisons between two groups performed using student's t-test. Data fitted with linear regression
1018 model and calculation of Pearson's correlation coefficient, presented as mean ± standard deviation (D, F)
1019 and mean ± standard error of the mean (B, C, E) . For C. & D. (CTRL: N=4 mice, n=8 cells; HFSD: N=2 mice,
1020 n=7 cells). For E.&F. (CTRL: N=6 mice, n = 16 cells; HFSD: N=6 mice, n=18 cells).
1021
1022
1023 **Fig. 6 Load dependence of cardiomyocyte Ca^{2+} transient decay in CTRL and HFSD cardiomyocytes.**
1024 **A-B.** Time constant of Ca^{2+} transient decay (tau) and time to peak Ca^{2+} transient in cardiomyocytes with
1025 different load conditions: loaded (L) & stretched (S) shown as fold change relative to non-loaded (N) for
1026 CTRL and HFSD.
1027 **C-D.** Exemplar Ca^{2+} transient decay records, with a mono-exponential decay function fit, in non-loaded and
1028 stretched CTRL and HFSD cardiomyocytes. Horizontal black broken lines intersect with mono-exponential fit
1029 at 36.8% (1/e) transient amplitude. Vertical broken lines from intersection points indicate the time constant
1030 of Ca^{2+} transient decay (tau).
1031
1032 For analysis of two independent variables a 2-way ANOVA with repeated measures used (CTRL: N = 5 mice,
1033 n = 13 cells; HFSD: N = 4 mice, n = 12 cells). Data are presented as mean ± standard deviation.
1034

1035 **Fig. 7 Pacing induced changes in cardiomyocyte cytosolic Ca^{2+} levels and stiffness in CTRL & HFSD.**
1036 **A.** Exemplar CTRL and HFSD cardiomyocyte Ca^{2+} transients at 2 and 4 Hz pacing.
1037 **B.** Diastolic cardiomyocyte Ca^{2+} levels measured before and after transition from 2 to 4 Hz pacing in HFSD &
1038 CTRL.
1039 **C.** Diastolic cardiomyocyte Ca^{2+} level mean shift with transition from 2 to 4 Hz pacing in HFSD & CTRL.
1040 **D.** Diastolic sarcomere length measured before and after transition from 2 to 4 Hz pacing in HFSD & CTRL.
1041 **E.** Diastolic mean cardiomyocyte segment stress-length relation (linear regression fit) for HFSD and CTRL at
1042 2 and 4 Hz pacing.
1043 **F.** Diastolic mean cardiomyocyte segment stress-length relation slope (mN/mm^2) normalized relative to
1044 segment stretch (% length) yields cardiomyocyte mean segment stress/strain = stiffness
1045 [(mN/mm^2) /strain (% length)] for HFSD and CTRL at 2 and 4 Hz pacing.
1046
1047 Comparison between two groups performed using unpaired t-test. With two independent variables a
1048 repeated measures 2-way ANOVA Sidaks post-hoc analysis was performed. Data are presented as mean ±
1049 standard deviation (C), mean ± standard error of the mean (E) or mean with paired individual points (B, D,
1050 F). For B. & C. (CTRL: N = 4 mice, n = 9 cells; HFSD: N = 4 mice, n = 8 cells). For D. & E. (CTRL: N = 4 mice, n =
1051 7 cells; HFSD: N = 4 mice, n = 9 cells). For F. (CTRL: N = 4 mice, n = 8 cells; HFSD: N = 4 mice, n = 9 cells).
1052
1053
1054
1055
1056

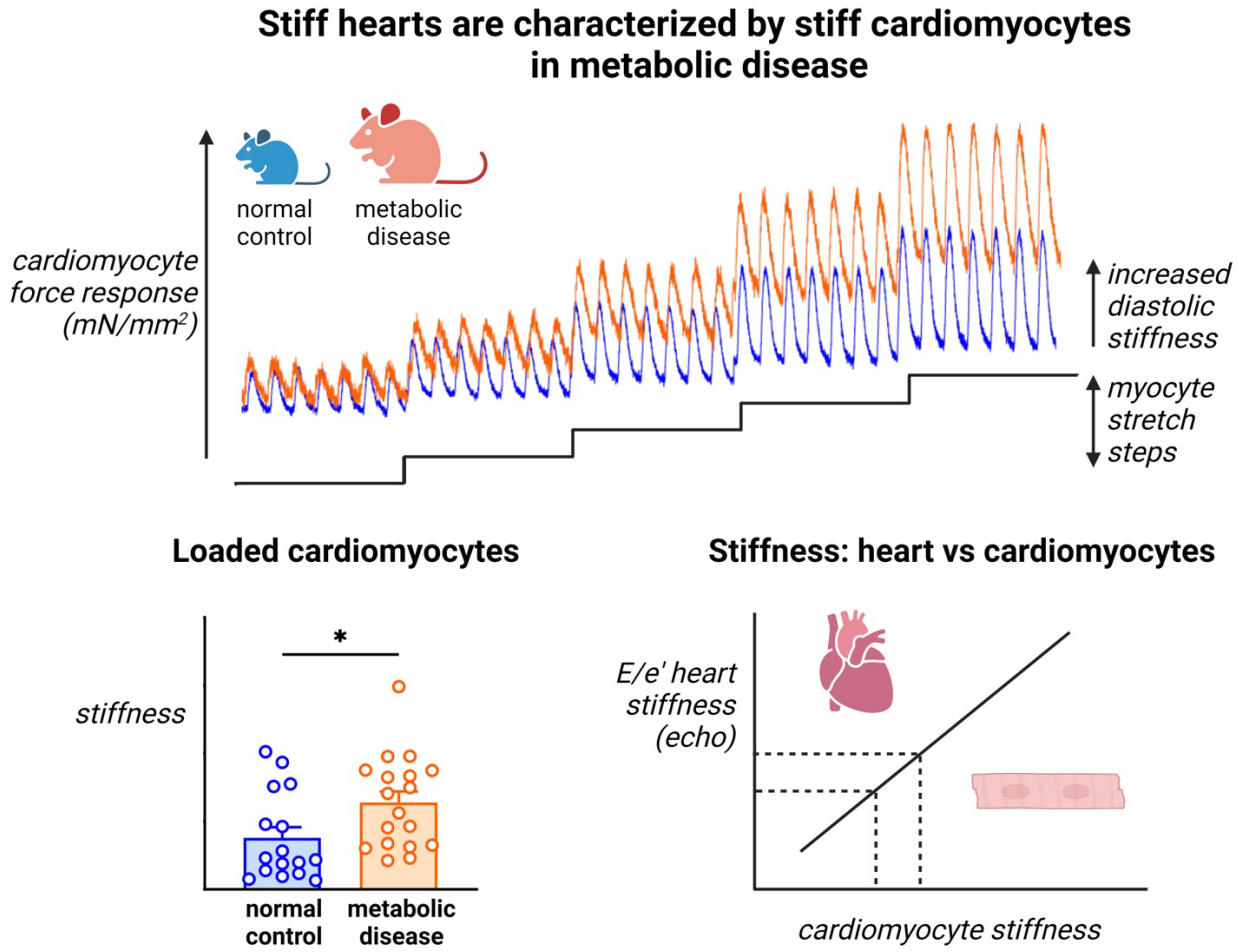

Abstract Figure Legend

Understanding cardiomyocyte stiffness components is an important priority for identifying new therapeutics for diastolic dysfunction, a key feature of cardiometabolic disease. In this study cardiac function was measured *in vivo* (echocardiography) for mice fed a high-fat/sugar diet (HFSD, ≥25weeks). Performance of intact isolated cardiomyocytes derived from the same hearts was measured during pacing under non-loaded, loaded and stretched conditions *in vitro.* Calibrated cardiomyocyte stretches demonstrated that stiffness was elevated in HFSD cardiomyocytes *in vitro* and correlated with diastolic dysfunction (E/e') *in vivo*. These findings show that stiff hearts are characterized by stiff cardiomyocytes in metabolic disease.

Table 1. Echocardiographic parameters for CTRL and HFSD mice

	CTRL	HFSD	P-value
Heart rate (bpm)	515±74	551±29	0.174
LV mass (mg)	125±27	131±21	0.314
LVIDd (mm)	3.60±0.17	4.16±0.47	0.004
IVSd (mm)	0.84±0.06	0.80±0.10	0.349
LVPWd (mm)	0.94±0.03	0.94±0.10	0.830
RWT (ratio)	0.49±0.06	0.43±0.09	0.079
Ejection Fraction (%)	67.8±3.7	64.9±3.2	0.093
Fractional Shortening (%)	31.8±3.6	30.6±2.1	0.400
E wave (mm/s)	472±74	569±65	0.003
A wave (mm/s)	348±99	400±116	0.190
e' wave (mm/s)	28.5±5.1	25.2±3.5	0.046
a' wave (mm/s)	23.5±7.8	23.5±6.4	0.995
E/A	1.51±0.41	1.47±0.37	0.095
e'/a'	1.33±0.44	1.12±0.39	0.171
E/e'	16.7±3.9	22.3±6.0	0.005
MV Deceleration Time (ms)	30.8±8.7	19.7±5.9	<0.001

Table 1. Echocardiographic parameters in CTRL and HFSD mice.
LVIDd left ventricular internal diameter at end diastole, *IVSd* interventricular septum diameter at end diastole, *LVPWd* left ventricular posterior wall thickness at end diastole, *RWT* relative wall thickness, *E wave* mitral valve blood flow velocity during the early ventricular filling phase, *A wave* mitral valve blood flow velocity during atrial contraction, *e' wave* mitral annulus tissue motion velocity during the early ventricular filling phase, *a' wave* mitral annulus tissue motion velocity during atrial contraction, *MV* mitral valve.

Comparisons between two treatment groups performed using Students' unpaired t-test (N = 9-15 mice per group). Data are presented as mean ± standard deviation.

Table 2. Stress-length relation mean values for CTRL and HFSD mouse cardiomyocytes

	CTRL 2 Hz	HFSD 2 Hz	p-value
Systolic Stress-SL Relation slope ((mN/mm^2) / µm)	6.54±4.97	16.35±15.09	0.087
Systolic Stress-Length Relation slope ((mN/mm^2) / %length)	0.013±0.011	0.022±0.011	0.022
Systolic : Diastolic Stress-SL relation 'Frank-Starling Gain Index' (ratio)	2.40±1.06	2.77±1.45	0.562
Systolic : Diastolic Stress-Length relation (ratio)	1.62±0.25	1.73±0.50	0.471

Table 2. Stress-length relation mean values for CTRL and HFSD mouse cardiomyocytes.
Comparisons between two treatment groups performed using Students' unpaired t-test (CTRL: N = 4-6 mice, n = 9-17 cells cells; HFSD: N = 2-6 mice, n = 7-19 cells). Data are presented as mean ± standard deviation.

Table 3. Ca^{2+} transient parameters for loaded CTRL and HFSD mouse cardiomyocytes

	CTRL 2 Hz	CTRL 4 Hz	HFSD 2 Hz	HFSD 4 Hz	Frequency p-value	Diet p-value	Interaction p-value
Systolic Ca^{2+} ($F_{340:380}$)	0.93±0.08	1.05±0.10#	0.99±0.15	1.08±0.20	p = 0.0004	p = 0.571	p = 0.100
Amplitude Ca^{2+} ($F_{340:380}$)	0.26±0.06	0.28±0.06	0.32±0.10	0.33±0.11	p = 0.569	p = 0.0672	p = 0.723
Time constant of Ca^{2+} decay (tau, sec)	0.21±0.07	0.09±0.02#	0.17±0.07	0.09±0.03#	p < 0.0001	p = 0.207	p = 0.350

Table 3. Ca^{2+} transient parameters for loaded CTRL and HFSD mouse cardiomyocytes.
Comparisons in data with two independent variable were performed using a mixed analysis 2-way ANOVA with Sidak's post-hoc analysis (CTRL, 2 Hz: N = 5 mice, n = 13 cells; CTRL, 4 Hz: N = 4 mice, n = 9 cells; HFSD, 2 Hz: N = 5 mice, n = 14 cells; HFSD, 4 Hz: N = 4 mice, n = 8 cells). Data are presented as mean ± standard deviation. P-values for ANOVA effects (Frequency, Diet, Interaction) are listed within the table. #<0.05: Significant pairwise post-hoc frequency differences vs CTRL 2 Hz or HFSD 2 Hz. No pairwise post-hoc treatment differences were observed.

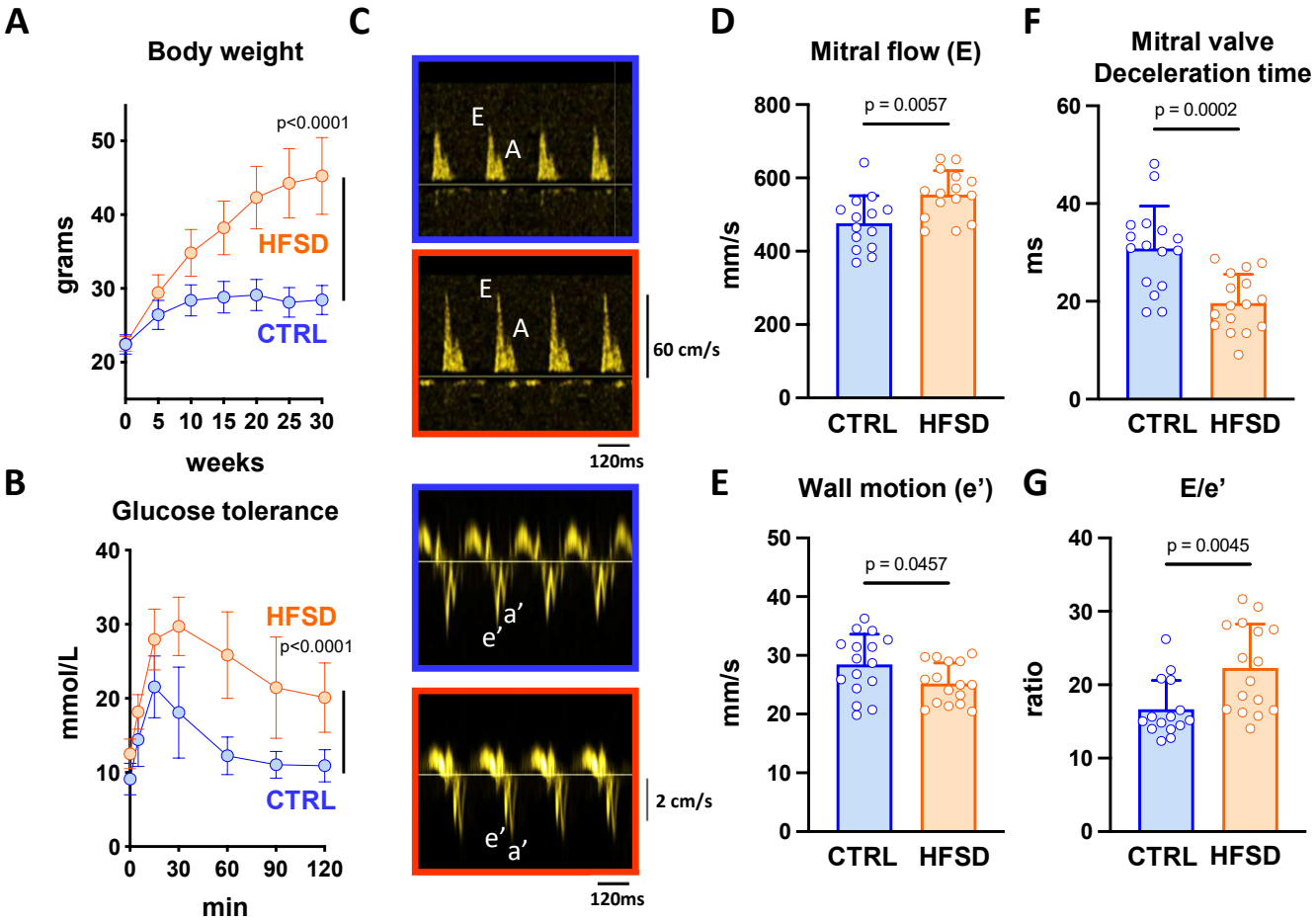

Fig.1 Systemic indicators of cardiometabolic disease and *in vivo* diastolic function in high-fat/sugar diet (HFSD) vs control (CTRL) mice.

A. Body weight elevation at 5 week intervals up to 30 weeks of dietary treatment (last timepoint full cohort intact. N = 16 – 17 mice per group).

B. Glucose tolerance testing at 23-24 weeks post dietary intervention; N = 6 mice per group).

C. Echocardiography exemplar blood flow and tissue doppler images from which diastolic indices were derived for CTRL and HFSD mice. Panels with orange outline: HFSD mitral blood flow & annular wall motion. Panels with blue outline: CTRL mitral blood flow & annular wall motion. (N = 14-16 mice per group)

D. Early diastolic mitral annular blood flow (E) was increased in HFSD.

E. Early diastolic mitral annular wall velocity (e') was decreased in HFSD.

F. Deceleration time of early diastolic mitral annular blood flow was decreased in HFSD.

G. Ratio of early diastolic blood flow to wall velocity (E/e') was increased in HFSD.

Time-course data analysed using two-way repeated measures ANOVA with Sidak post-hoc test with p-value for 'time x diet' effect presented. Comparisons between two treatment groups performed using student's t-test. Data presented as mean ± standard deviation.

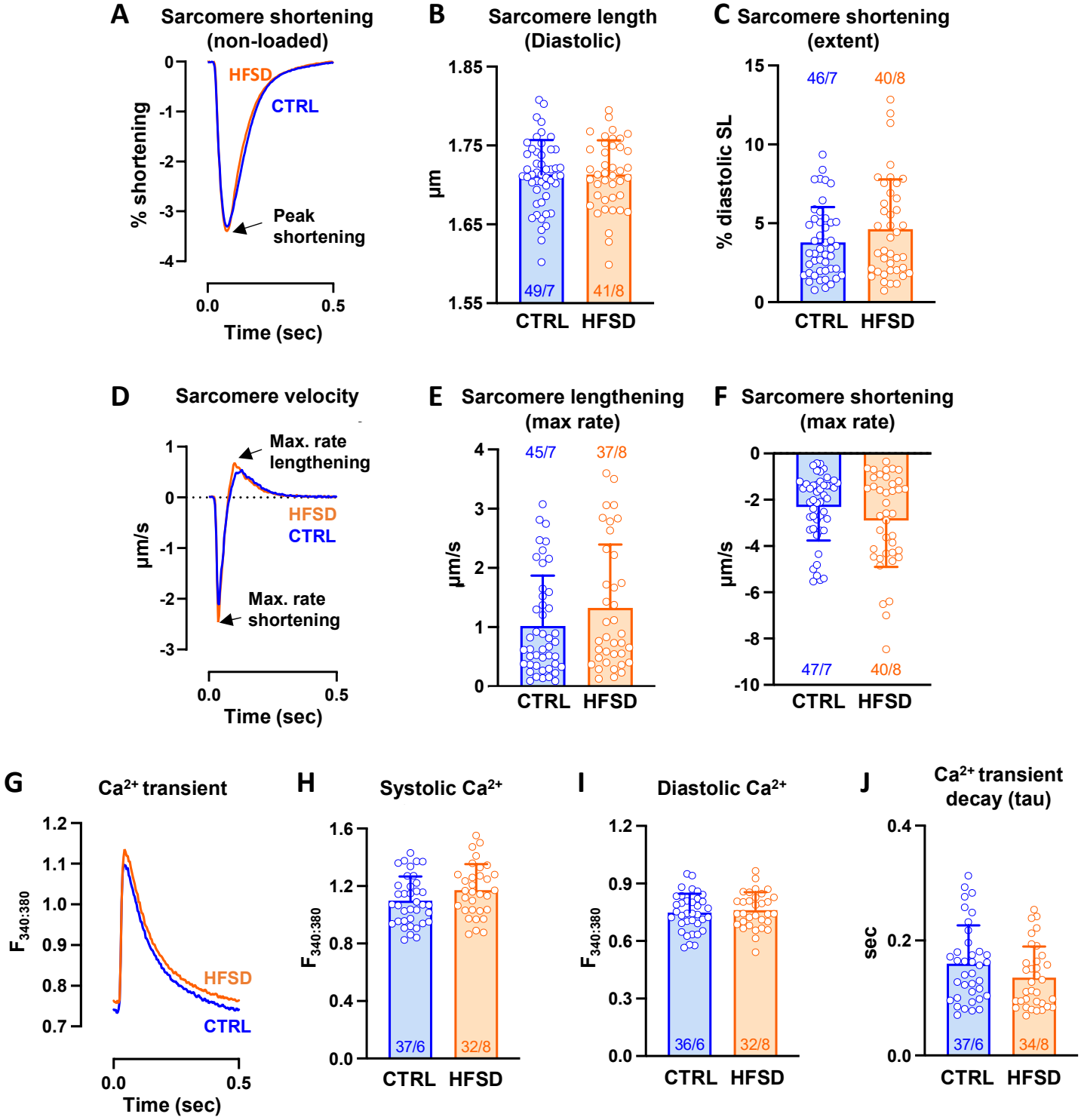
A
Sarcomere shortening (non-loaded)
% shortening
HFSD
CTRL
Peak shortening
Time (sec)
B
Sarcomere length (Diastolic)
µm
49/7
41/8
CTRL HFSD
C
Sarcomere shortening (extent)
% diastolic SL
46/7
40/8
CTRL HFSD
D
Sarcomere velocity
µm/s
Max. rate lengthening
HFSD
CTRL
Max. rate shortening
Time (sec)
E
Sarcomere lengthening (max rate)
µm/s
45/7
37/8
CTRL HFSD
F
Sarcomere shortening (max rate)
µm/s
47/7
40/8
CTRL HFSD
G
Ca2+ transient
F340:380
HFSD
CTRL
Time (sec)
H
Systolic Ca2+
F340:380
37/6
32/8
CTRL HFSD
I
Diastolic Ca2+
F340:380
36/6
32/8
CTRL HFSD
J
Ca2+ transient decay (tau)
sec
37/6
34/8
CTRL HFSD

Fig.2 Non-loaded sarcomere and Ca^{2+} dynamics in CTRL and HFSD cardiomyocytes.
A. Mean sarcomere contraction cycles presented as a percentage of diastolic sarcomere length for CTRL and HFSD cardiomyocytes
B-C. Mean diastolic sarcomere length and extent of sarcomere shortening for CTRL and HFSD cardiomyocytes.
D. Mean sarcomere shortening and lengthening rate records (time derivative of sarcomere contraction-relaxation cycle) for CTRL and HFSD cardiomyocytes. The nadir and zenith represent maximal shortening and lengthening rates respectively.
E-F. Maximal rate of lengthening and shortening rates for CTRL and HFSD cardiomyocytes.
G. Mean Ca^{2+} transient records for CTRL and HFSD cardiomyocytes.
H-J. Mean Ca^{2+} levels (systolic and diastolic) and time constant of transient decay (*tau*) in HFSD and CTRL cardiomyocytes.

Mean data computed from average of 20 cycles per cardiomyocyte to derive group mean (N = 6-8 mice per group, n = 32-49 cells per group). Comparisons between two treatment groups performed using student's t-test (all $p>0.05$, ns). Data presented as mean $\pm$ standard deviation.

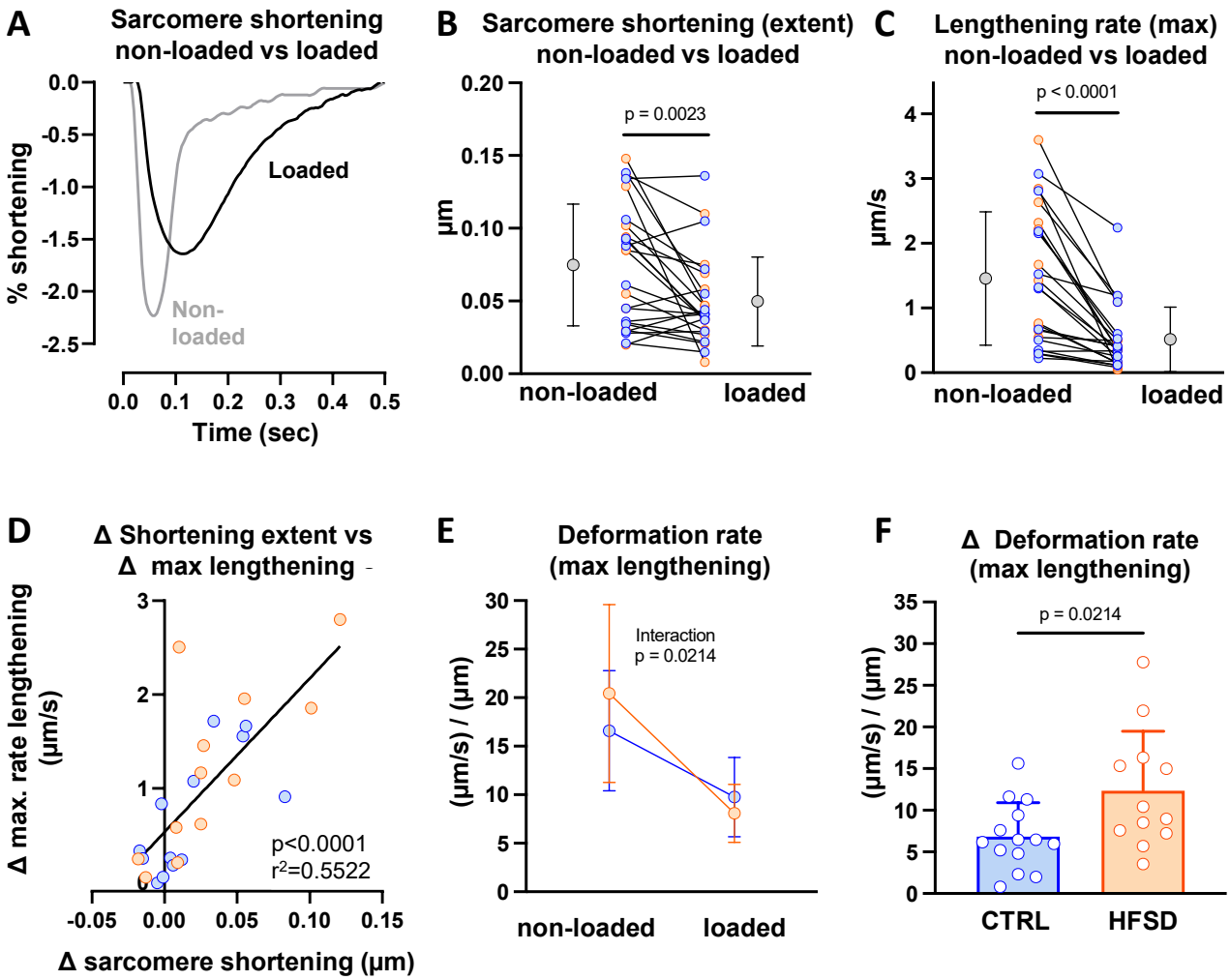

Fig. 3 Sarcomere shortening and lengthening in non-loaded and loaded pacing states.
A. Exemplar non-loaded and loaded sarcomere contraction cycles for the same cardiomyocyte (CTRL).
B-C. Extent of sarcomere shortening and maximum rate of lengthening, measured for each cardiomyocyte in non-loaded and loaded state for CTRL and HFSD groups combined (N = 9 mice, n = 25 cells). Mean data for CTRL and HFSD are presented as grey points to the left (non-loaded) and right (loaded) of individual cardiomyocyte data.
D. Correlation of loading associated sarcomere shortening change and maximum rate of lengthening change for CTRL and HFSD combined.
E. Mean loading effect on maximum deformation rate during lengthening ((µm/s) / µm; maximum rate of lengthening (µm/s) normalized by shortening extent (µm)) for CTRL vs HFSD. (CTRL: N = 5 mice, n = 14 cells; HFSD: N = 4 mice, n = 12 cells). Significant ANOVA interaction effect (diet treatment x load state).
F. Mean decrement in deformation rate during lengthening ((µm/s) / µm).

Comparison of cardiomyocyte responses in different loading conditions analysed by paired t-test. Comparison of cardiomyocytes from different treatment groups analysed by unpaired t-test. A 2-way ANOVA with repeated measures used for analysis of two independent variables. Data fitted with linear regression model and calculation of Pearson's correlation coefficient. Data presented as mean ± standard deviation.

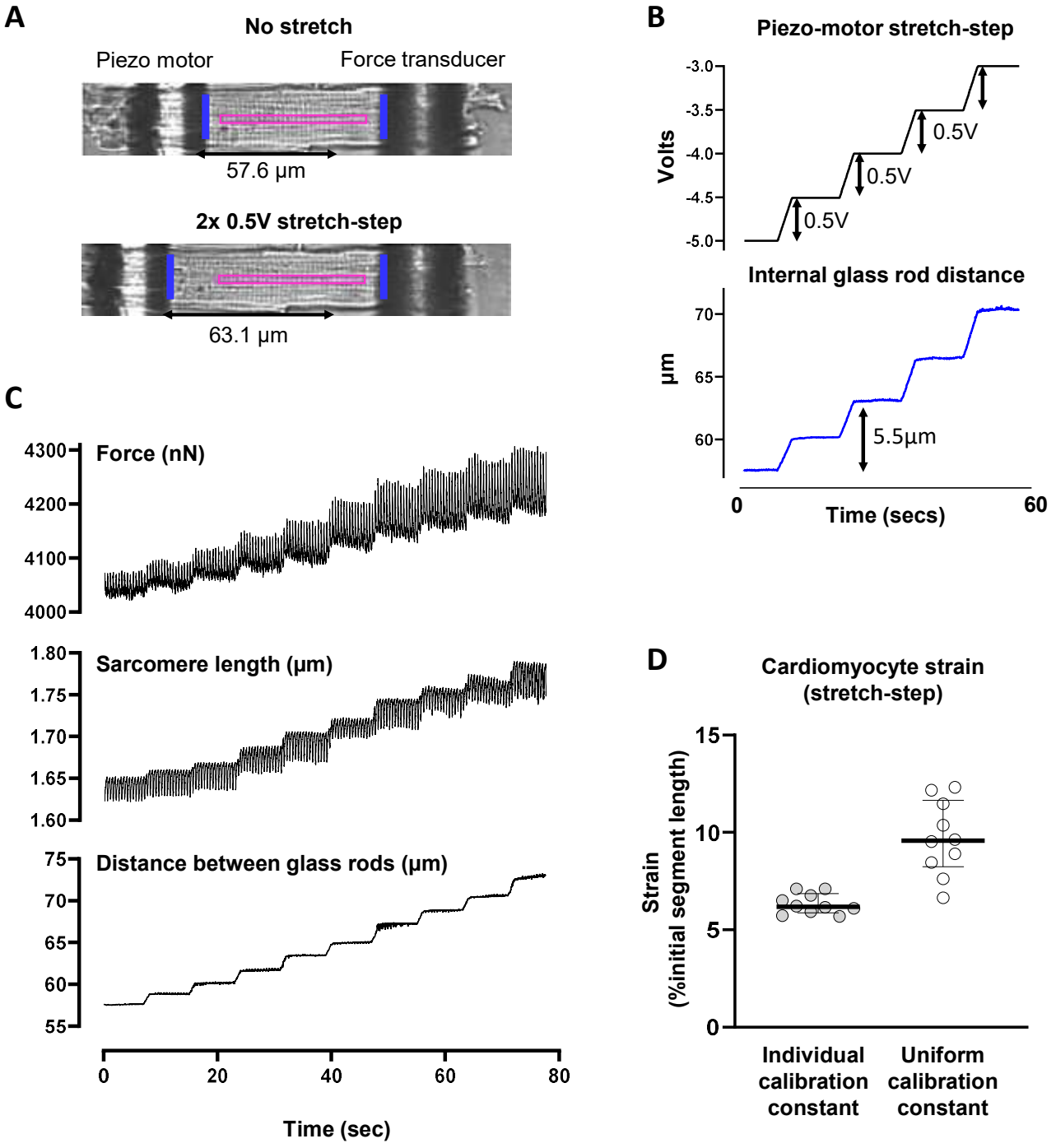

Fig. 4. Cardiomyocyte standardized stretch protocol.
A. Image of a left ventricular cardiomyocyte longitudinally attached to glass rods. Edge-tracking used to measure inter-rod distance (marked as blue bars) for cardiomyocyte segment analyses. The delineated region of interest (marked pink) represents the area from which Fast Fourier Transform analysis of sarcomere striations was performed to derive sarcomere-specific data.
B. Exemplar traces depict the change in glass rod internal distance in response to successive 0.5V piezo motor inputs used for calibration of stretch protocol for each individual cardiomyocyte to allow normalized comparisons.
C. Measuring stress and strain during progressive cardiomyocyte stretch. Exemplar force, sarcomere length and rod edge-tracker traces during the first stretch of a stress-length protocol.
D. Comparison of variability of cell stretches performed using a uniform (preset) stretch constant and the individually derived stretch calibration constant. Strain was measured as the %change in segment length relative to the initial segment length. Reproducibility is optimized using the individual stretch calibration constant. Data shown as median ± interquartile range.

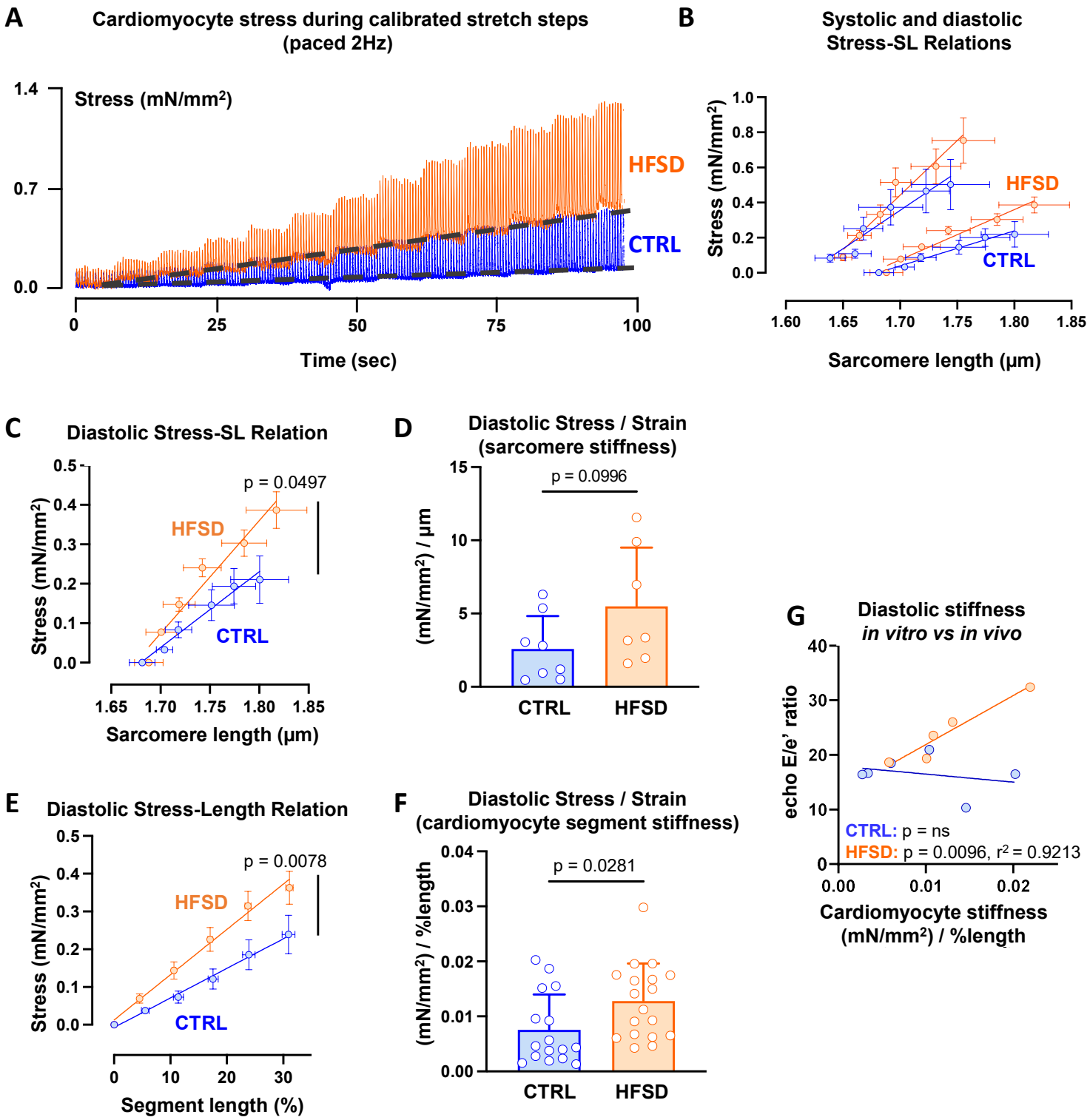
A
Cardiomyocyte stress during calibrated stretch steps
(paced 2Hz)
Stress (mN/mm²)
1.4
0.7
0.0
HFSD
CTRL
0
25
50
75
100
Time (sec)
B
Systolic and diastolic
Stress-SL Relations
Stress (mN/mm²)
1.0
0.8
0.6
0.4
0.2
0.0
HFSD
CTRL
1.60
1.65
1.70
1.75
1.80
1.85
Sarcomere length (µm)
C
Diastolic Stress-SL Relation
Stress (mN/mm²)
0.5
0.4
0.3
0.2
0.1
0.0
p = 0.0497
HFSD
CTRL
1.65
1.70
1.75
1.80
1.85
Sarcomere length (µm)
D
Diastolic Stress / Strain
(sarcomere stiffness)
(mN/mm²) / µm
15
10
5
0
p = 0.0996
CTRL
HFSD
G
Diastolic stiffness
in vitro vs in vivo
echo E/e' ratio
40
30
20
10
0
CTRL: p = ns
HFSD: p = 0.0096, r² = 0.9213
0.00
0.01
0.02
Cardiomyocyte stiffness
(mN/mm²) / %length
E
Diastolic Stress-Length Relation
Stress (mN/mm²)
0.5
0.4
0.3
0.2
0.1
0.0
p = 0.0078
HFSD
CTRL
0
10
20
30
Segment length (%)
F
Diastolic Stress / Strain
(cardiomyocyte segment stiffness)
(mN/mm²) / %length
0.04
0.03
0.02
0.01
0.00
p = 0.0281
CTRL
HFSD

Fig. 5 Quantifying diastolic stiffness in CTRL vs HFSD cardiomyocytes using strain normalization methods
A. Exemplar stress recordings of CTRL and HFSD cardiomyocytes undergoing 'stress-length' protocol (2Hz paced). Diastolic baseline stress shifts indicated by broken line.
B. Diastolic (pair of lower lines) and systolic (pair of upper lines) sarcomere mean stress- sarcomere length (SL) relations in CTRL cardiomyocytes (N = 5 mice, n = 9 cells).
C. Diastolic mean stress-sarcomere length relation (linear regression fit) for HFSD and CTRL.
D. Diastolic stress (mN/mm^2) normalized relative to sarcomere stretch (µm) yields sarcomere stress/strain = stiffness [(mN/mm^2) /strain (µm)] for HFSD and CTRL.
E. Diastolic mean cardiomyocyte segment stress-length relation (linear regression fit) for HFSD and CTRL..
F. Diastolic stress (mN/mm^2) normalized relative to segment stretch (% length) yields cardiomyocyte segment stress/strain = stiffness [(mN/mm^2) /strain (% length)] for HFSD & CTRL.
G. Correlation (linear regression fit) of *in vitro* cardiomyocyte segment diastolic stiffness (stress/strain) with *in vivo* diastolic dysfunction E/e' (blood flow/wall motion) in CTRL and HFSD. Cardiomyocyte data averaged per heart.

Comparisons between two groups performed using student's t-test. Data fitted with linear regression model and calculation of Pearson's correlation coefficient, presented as mean ± standard deviation (D, F) and mean ± standard error of the mean (B, C, E) . For **C. & D.** (CTRL: N=4 mice, n=8 cells; HFSD: N=2 mice, n=7 cells). For **E.&F.** (CTRL: N=6 mice, n = 16 cells; HFSD: N=6 mice, n=18 cells).

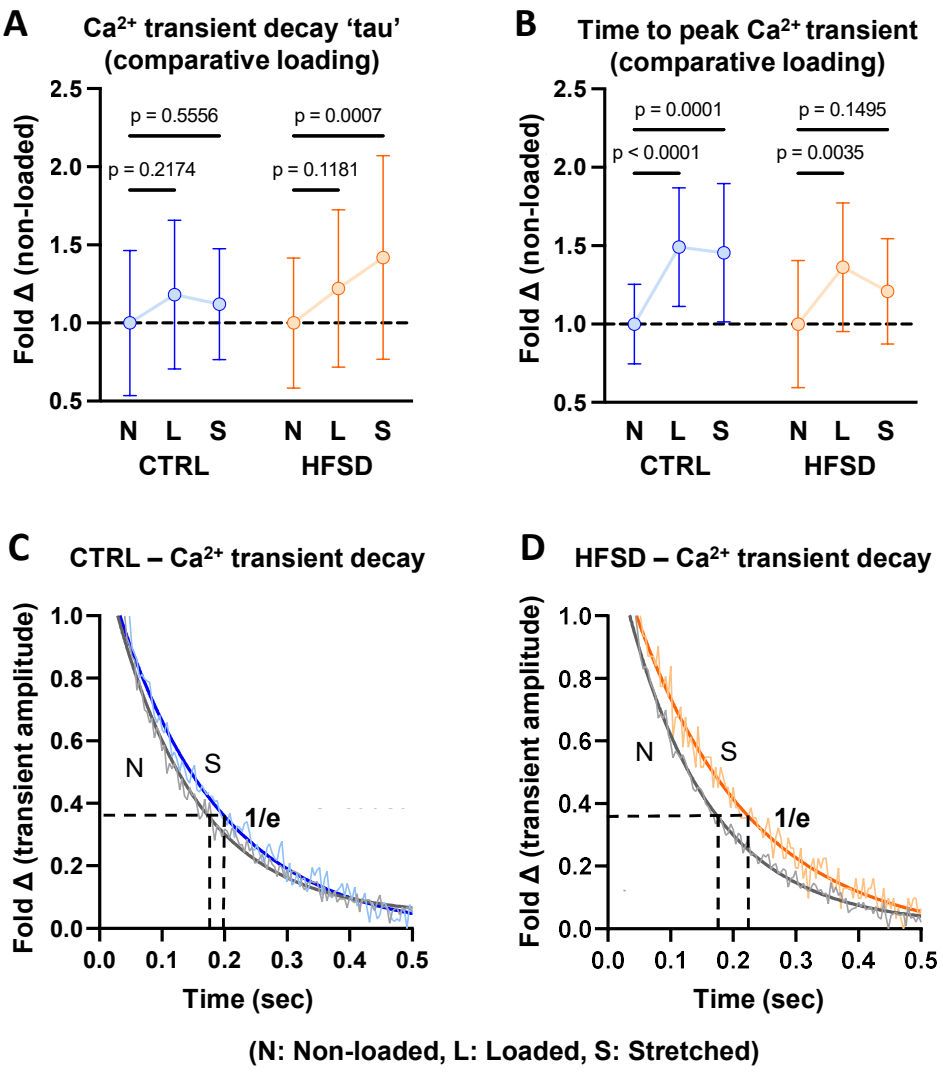

Fig. 6 Load dependence of cardiomyocyte Ca^{2+} transient decay in CTRL and HFSD cardiomyocytes.

A-B. Time constant of Ca^{2+} transient decay (tau) and time to peak Ca^{2+} transient in cardiomyocytes with different load conditions: loaded (L) & stretched (S) shown as fold change relative to non-loaded (N) for CTRL and HFSD.
C-D. Exemplar Ca^{2+} transient decay records, with a mono-exponential decay function fit, in non-loaded and stretched CTRL and HFSD cardiomyocytes. Horizontal black broken lines intersect with mono-exponential fit at 36.8% (1/e) transient amplitude. Vertical broken lines from intersection points indicate the time constant of Ca^{2+} transient decay (tau).

For analysis of two independent variables a 2-way ANOVA with repeated measures used (CTRL: N = 5 mice, n = 13 cells; HFSD: N = 4 mice, n = 12 cells). Data are presented as mean ± standard deviation.

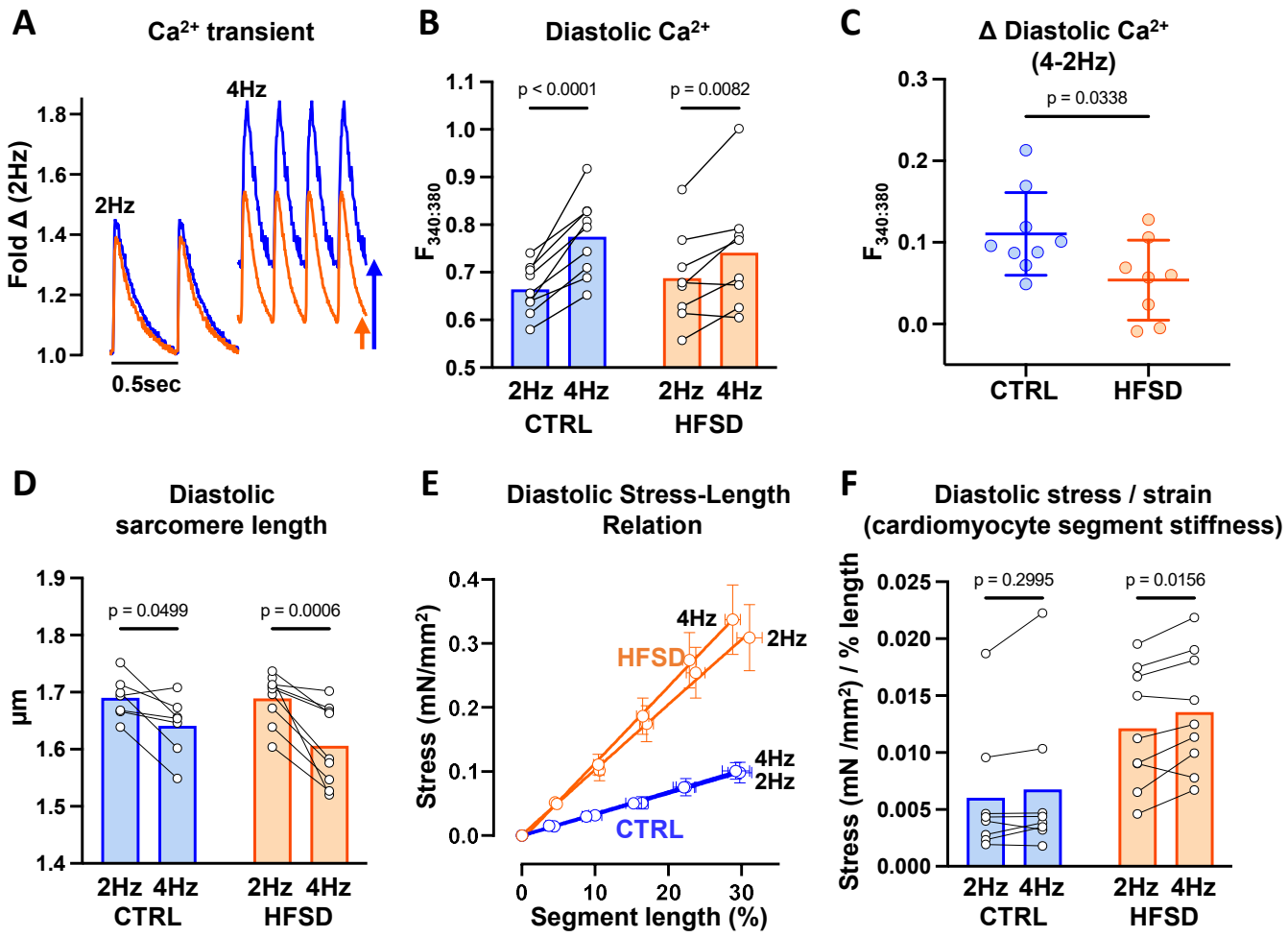

Fig. 7 Pacing induced changes in cardiomyocyte cytosolic Ca^{2+} levels and stiffness in CTRL & HFSD.
A. Exemplar CTRL and HFSD cardiomyocyte Ca^{2+} transients at 2 and 4 Hz pacing.
B. Diastolic cardiomyocyte Ca^{2+} levels measured before and after transition from 2 to 4 Hz pacing in HFSD & CTRL.
C. Diastolic cardiomyocyte Ca^{2+} level mean shift with transition from 2 to 4 Hz pacing in HFSD & CTRL.
D. Diastolic sarcomere length measured before and after transition from 2 to 4 Hz pacing in HFSD & CTRL.
E. Diastolic mean cardiomyocyte segment stress-length relation (linear regression fit) for HFSD and CTRL at 2 and 4 Hz pacing.
F. Diastolic mean cardiomyocyte segment stress-length relation slope (mN/mm^2) normalized relative to segment stretch (% length) yields cardiomyocyte mean segment stress/strain = stiffness [(mN/mm^2) /strain (% length)] for HFSD and CTRL at 2 and 4 Hz pacing.

Comparison between two groups performed using unpaired t-test. With two independent variables a repeated measures 2-way ANOVA Sidaks post-hoc analysis was performed. Data are presented as mean ± standard deviation (C), mean ± standard error of the mean (E) or mean with paired individual points (B, D, F). For **B. & C.** (CTRL: N = 4 mice, n = 9 cells; HFSD: N = 4 mice, n = 8 cells). For **D. & E.** (CTRL: N = 4 mice, n = 7 cells; HFSD: N = 4 mice, n = 9 cells). For **F.** (CTRL: N = 4 mice, n = 8 cells; HFSD: N = 4 mice, n = 9 cells).

Table 1. Echocardiographic parameters for CTRL and HFSD mice			
	CTRL	**HFSD**	**P-value**
Heart rate (bpm)	515±74	551±29	0.174
LV mass (mg)	125±27	131±21	0.314
LVIDd (mm)	3.60±0.17	4.16±0.47	0.004
IVSd (mm)	0.84±0.06	0.80±0.10	0.349
LVPWd (mm)	0.94±0.03	0.94±0.10	0.830
RWT (ratio)	0.49±0.06	0.43±0.09	0.079
Ejection Fraction (%)	67.8±3.7	64.9±3.2	0.093
Fractional Shortening (%)	31.8±3.6	30.6±2.1	0.400
E wave (mm/s)	472±74	569±65	0.003
A wave (mm/s)	348±99	400±116	0.190
e' wave (mm/s)	28.5±5.1	25.2±3.5	0.046
a' wave (mm/s)	23.5±7.8	23.5±6.4	0.995
E/A	1.51±0.41	1.47±0.37	0.095
e'/a'	1.33±0.44	1.12±0.39	0.171
E/e'	16.7±3.9	22.3±6.0	0.005
MV Deceleration Time (ms)	30.8±8.7	19.7±5.9	<0.001

Table 1. Echocardiographic parameters in CTRL and HFSD mice.
LVIDd left ventricular internal diameter at end diastole, *IVSd* interventricular septum diameter at end diastole, *LVPWd* left ventricular posterior wall thickness at end diastole, *RWT* relative wall thickness, *E wave* mitral valve blood flow velocity during the early ventricular filling phase, *A wave* mitral valve blood flow velocity during atrial contraction, *e' wave* mitral annulus tissue motion velocity during the early ventricular filling phase, *a' wave* mitral annulus tissue motion velocity during atrial contraction, *MV* mitral valve.

Comparisons between two treatment groups performed using Students' unpaired t-test (N = 9-15 mice per group). Data are presented as mean ± standard deviation.

Table 2. Stress-length relation mean values for CTRL and HFSD mouse cardiomyocytes			
	CTRL 2 Hz	**HFSD 2 Hz**	**p-value**
Systolic Stress-SL Relation slope ((mN/mm^2) / µm)	6.54±4.97	16.35±15.09	0.087
Systolic Stress-Length Relation slope ((mN/mm^2) / %length)	0.013±0.011	0.022±0.011	0.022
Systolic : Diastolic Stress-SL relation 'Frank-Starling Gain Index' (ratio)	2.40±1.06	2.77±1.45	0.562
Systolic : Diastolic Stress-Length relation (ratio)	1.62±0.25	1.73±0.50	0.471

Table 2. Stress-length relation mean values for CTRL and HFSD mouse cardiomyocytes.
Comparisons between two treatment groups performed using Students' unpaired t-test (CTRL: N = 4-6 mice, n = 9-17 cells cells; HFSD: N = 2-6 mice, n = 7-19 cells). Data are presented as mean ± standard deviation.

Table 3. Ca^{2+} transient parameters for loaded CTRL and HFSD mouse cardiomyocytes

	CTRL 2 Hz	CTRL 4 Hz	HFSD 2 Hz	HFSD 4 Hz	Frequency p-value	Diet p-value	Interaction p-value
Systolic Ca^{2+} ($F_{340:380}$)	0.93±0.08	1.05±0.10#	0.99±0.15	1.08±0.20	p = 0.0004	p = 0.571	p = 0.100
Amplitude Ca^{2+} ($F_{340:380}$)	0.26±0.06	0.28±0.06	0.32±0.10	0.33±0.11	p = 0.569	p = 0.0672	p = 0.723
Time constant of Ca^{2+} decay (tau, sec)	0.21±0.07	0.09±0.02#	0.17±0.07	0.09±0.03#	p < 0.0001	p = 0.207	p = 0.350

Table 3. Ca^{2+} transient parameters for loaded CTRL and HFSD mouse cardiomyocytes.
Comparisons in data with two independent variable were performed using a mixed analysis 2-way ANOVA with Sidak's post-hoc analysis (CTRL, 2 Hz: N = 5 mice, n = 13 cells; CTRL, 4 Hz: N = 4 mice, n = 9 cells; HFSD, 2 Hz: N = 5 mice, n = 14 cells; HFSD, 4 Hz: N = 4 mice, n = 8 cells). Data are presented as mean ± standard deviation. P-values for ANOVA effects (Frequency, Diet, Interaction) are listed within the table. #<0.05: Significant pairwise post-hoc frequency differences vs CTRL 2 Hz or HFSD 2 Hz. No pairwise post-hoc treatment differences were observed.